

# Studying the Contribution of the Perivascular Space on Diffusion-Weighted Imaging

Callum Coffey

Thesis submitted for the degree of  
Master of Science in  
Biomedical Engineering, option  
Bio-Informatics and AI

**Supervisor:**  
Prof. dr. ir. Daan Christiaens

**Co-Supervisors:**  
Dr. Louise Emsell  
Prof. dr. M. Van Den Bossche

**Assessors:**  
Dr. A. Radwan  
Prof. dr. ir. F. Maes

© Copyright KU Leuven

Without written permission of the supervisor and the author it is forbidden to reproduce or adapt in any form or by any means any part of this publication. Requests for obtaining the right to reproduce or utilize parts of this publication should be addressed to Faculteit Ingenieurswetenschappen, Kasteelpark Arenberg 1 bus 2200, B-3001 Leuven, +32-16-321350.

A written permission of the supervisor is also required to use the methods, products, schematics and programmes described in this work for industrial or commercial use, and for submitting this publication in scientific contests.

# Preface

I would like to thank my supervisors, Prof. Daan Christiaens and Dr. Louise Emsell for their guidance, expertise, and constant support. Their encouragement and feedback have been invaluable in shaping this research.

I would like to thank my parents for helping me become the person I am today. Finally, I would like to express my adoration and appreciation to Sai for all the love and support these past seven years, and without whom I could not have gotten this far.

*Callum Coffey*

# Abstract

Perivascular spaces (PVS) play a critical role in the brain's vascular and waste removal systems. Despite the existence of local metrics like DTI-ALPS, there is currently a lack of an automated global model for evaluating PVS. This study aimed to fill that gap by developing a global diffusion metric for the PVS, derived from high-resolution structural imaging combined with diffusion-weighted imaging (DWI). The segmentation of PVS was performed using the Weakly-supervised Perivascular Space Segmentation (WPSS) method and validated through a customized visual scoring approach. PVS orientation was estimated by applying a Hessian-based filter to determine the direction of minimum curvature. A multi-tensor model constrained by the orientation field was formulated to characterize PVS diffusion, which demonstrated stable and consistent performance in-vivo across the entire brain. The model was further evaluated on synthetic data, confirming its stability across a wide range of physiologically relevant conditions. This study provides a significant advancement in directly quantifying diffusion metrics from the PVS, simplifying the modeling process by integrating both PVS location and orientation.

# Contents

<b>Preface</b>	<b>i</b>
<b>Abstract</b>	<b>ii</b>
<b>List of Abbreviations</b>	<b>iv</b>
<b>List of Figures and Tables</b>	<b>v</b>
<b>1 Introduction</b>	<b>1</b>
1.1 Problem Statement . . . . .	1
1.2 Perivascular Spaces: Structure, Function, and Transport . . . . .	2
1.3 State-of-Art . . . . .	5
1.4 Datasets . . . . .	8
<b>2 Structural Analysis of PVS</b>	<b>9</b>
2.1 Background . . . . .	9
2.2 Segmentation . . . . .	12
2.3 Validation . . . . .	15
2.4 Capturing Orientation . . . . .	18
<b>3 Modelling PVS Diffusion</b>	<b>21</b>
3.1 Background . . . . .	21
3.2 Diffusivity Metrics . . . . .	28
3.3 Simulation . . . . .	34
<b>4 Discussion</b>	<b>40</b>
4.1 Segmentation . . . . .	40
4.2 Evaluating the Constrained-Multi-Tensor Model . . . . .	41
4.3 Next Steps . . . . .	42
4.4 Conclusion . . . . .	44
<b>A Supplemental Results</b>	<b>45</b>
<b>Bibliography</b>	<b>49</b>

# List of Abbreviations

## Abbreviations

**AQP4** Aquaporin-4.

**CSD** Constrained Spherical Deconvolution.

**DWI** Diffusion-Weighted Imaging.

**EPC** Enhanced Perivascular Contrast.

**fODF** Fiber Orientation Distribution Function.

**GDBA** Gadolinium-based Agents.

**IPAD** Intramural Periarterial Drainage.

**MSMT** Multi-Shell Multi-Tissue.

**PVS** Perivascular Space.

**QSM** Quantitative Susceptibility Mapping.

**SAS** Subarachnoid Space.

**SWI** Susceptibility-Weighted Imaging.

**WPSS** Weakly-supervised Perivascular Space Segmentation.

# List of Figures and Tables

## List of Figures

1.1 Comparison of periarterial and perivenous spaces . . . . .	3
1.2 DTI-ALPS Background and Methodology . . . . .	7
2.1 Network Architecture of WPSS . . . . .	14
2.2 Comparison of EPC with SWI . . . . .	18
2.3 PCA vs Hessian Orientation Phantoms . . . . .	19
2.4 Hessian-based PVS Orientation . . . . .	20
3.1 PGSE Sequence with Phase Evolution . . . . .	22
3.2 DTI vs fODF of PVS . . . . .	29
3.3 Magnitude of PVS-matching and largest 5 fODF peaks . . . . .	30
3.4 Comparison of Single-Tensor and Multi-Tensor Diffusion Models . . . . .	33
3.5 Simulation of Single Compartment Tensor Reconstruction. . . . .	38
3.6 Comparison of Single-Tensor and Multi-Tensor Diffusion Models . . . . .	39
A.1 Results of Multi-Tensor Simulation . . . . .	45
A.2 Simulation of Single Compartment Tensor Reconstruction. . . . .	46
A.3 Simulation of Single Compartment Tensor Reconstruction. . . . .	47

## List of Tables

3.1 Summary statistics for in-vivo application of PVS Models. . . . .	33
3.2 List of parameters and degrees of freedom (DOF) for the Single-Tensor, Multi-Tensor, and Constrained Multi-Tensor Models. Total DOF is the sum of all independent parameters. . . . .	37
3.3 Parameter Ranges and Defaults for Experiments . . . . .	37
A.1 Visual Scoring of Perivascular Space Segmentation . . . . .	48

# Chapter 1

## Introduction

This chapter provides an overview of the perivascular space (PVS), focusing on its physiology, pathology, and the current state-of-the-art imaging techniques used to assess it. We will also introduce the imaging modalities employed in this study and briefly describe the datasets from which the data were sourced. To structure the thesis, the background, methods, and results are divided across four chapters. The current chapter serves as the introduction. The following chapter will focus on the segmentation techniques used to estimate the orientation of the PVS, generating a vector field that will be crucial for subsequent analysis. The third chapter will present the diffusion methods, using the PVS orientation to derive diffusion metrics, simulate them, and explore their implications. Finally, the fourth chapter will discuss the integrated results, review alternative methods, and consider future directions for research.

### 1.1 Problem Statement

Perivascular spaces, a broad term for fluid filled spaces surrounding small vessels in the brain, represent one of the most novel and exciting areas of research in neuroscience. These spaces play a crucial role in the brain's waste clearance systems. Recent studies have correlated enlarged PVS with various neurodevelopmental and neurodegenerative disorders. However, enlargement also occurs in non-pathological tissue, suggesting a more complex link between enlarged PVS and its comorbidities. It is believed that this enlargement is caused by disruptions in diffusion rates, potentially caused by buildup of neurotoxic waste byproducts such as beta-amyloid. Despite their significance, research into the PVS is hindered by an absence of non-invasive global automated methods for analyzing quantitative imaging data. [1]

A crucial first step toward addressing this gap is the development of a robust segmentation method. In typical segmentation tasks, such as for the corpus callosum, prior knowledge of tissue physiology and morphology enables the use of anatomical landmarks or heuristic filters. This is made possible by significant inter-patient correlations and the continuous shape of the tissue. Unfortunately, PVS segmentation presents unique challenges: large portions of the PVS are sub-voxel in

## 1.2. Perivascular Spaces: Structure, Function, and Transport

---

scale, making it impossible to segment entire vessels from end to end using current imaging techniques. Additionally, PVS exhibit no consistent symmetry, lack clear intra-patient correlations, and vary significantly in physiology and surrounding tissue composition across regions. These factors necessitate the development of more advanced segmentation tools capable of capturing PVS structure across the whole brain, not just in idealized regions. The second component is measuring the tissue. Diffusion MRI is a fantastic tool for obtaining quantitative measures of the PVS but suffers from lower resolution relative to structural MRI. Methods such as DTI-ALPS exist which make use of diffusion MRI without a segmentation. However, they rely on small regions of well understood physiology so they are only capable of quantifying a local model of diffusion behavior. The clear next step is a global method which can quantify PVS diffusivity across the entire brain. [2, 3]

The novelty of this study is combining the structural and diffusion MRI modalities to obtain higher resolution spatial information which can then be used to quantify the diffusion along the PVS. First high resolution structural data will be used to obtain a segmentation. This segmentation allows for estimating the voxel-wise orientation of the perivascular space. Given that the resolution of current diffusion techniques is not sufficient for precise segmentation or for distinguishing diffusion orientations, combining these modalities should allow for more accurate modeling of the PVS.

## 1.2 Perivascular Spaces: Structure, Function, and Transport

Perivascular spaces, also known as Virchow-Robins spaces, are the fluid filled space surrounding arterioles, venules, and capillaries in the brain. They have a role in the exchange of solutes between ISF and CSF, along with transport of CSF deeper into the brain. The spaces are limited by the astrocytic endfeet which helps form the tight cell junction necessary for the blood-brain barrier. [4]

The PVS can be divided into 3 regions, perivenous spaces, periarterial spaces and pericapillary spaces, surrounding venules, arterioles, and capillaries respectively. The spaces around capillaries are so small that they are functionally negligible to imaging. The majority of research focuses on perivenous and periarterial spaces, often not distinguishing between them. The difference between periarterial and perivenous is visible in Figure 1.1. To preserve integrity of the blood brain barrier the PVS does not directly communicate with the SAS. Instead it is sheathed within the semi-permeable pia mater which regulates fluid exchange. However, unlike perivenous spaces, the periarterial spaces have a reflected layer of pia mater which continues along the vessel. As you proceed along the vessel you encounter more gaps in this layer, leptomeningeal perforations. These gaps grow larger and more numerous until the reflected Pia mater is no longer present, somewhere between periarterial and pericapillary. It should be noted that the inner and outer periarterial spaces are continuous with each other and the perivenous spaces so the composition of solutes on both sides of the reflected pia mater should be similar. There are some notable exceptions to their physiology. There is no PVS surrounding cortical arteries

## 1.2. Perivascular Spaces: Structure, Function, and Transport

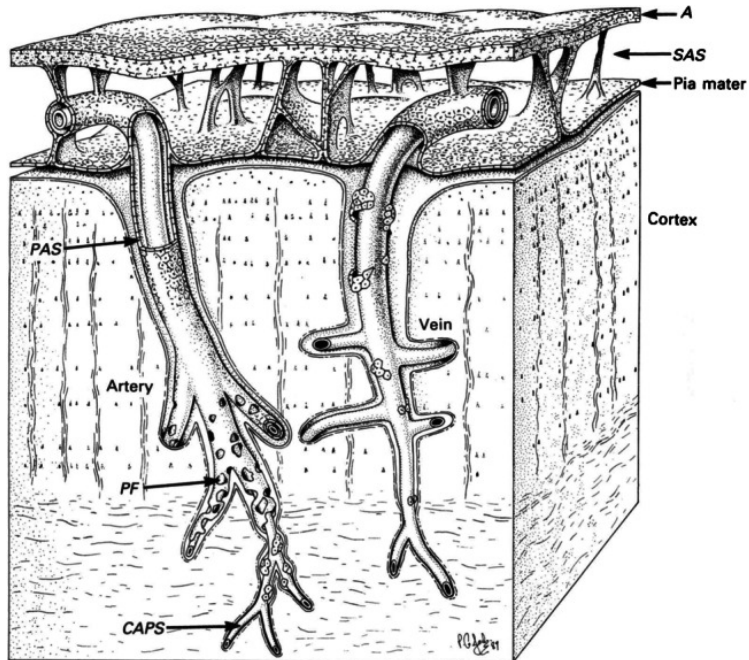


FIGURE 1.1: Schematic representation of PVS surrounding penetrating vessels at the border of the sub arachnoid space(SAS). The periarterial space clearly show the gradual increase of leptomeningeal perforations(PF). [1, 5]

and the periarterial spaces near the basal ganglia have two layers of reflected pia mater. [1]

The role of the PVS as a waste clearance mechanism necessitates a faster flow rate than simple diffusion. The mechanisms which drive flow through the PVS are not fully understood but several key factors have been identified. The largest contributor to flow through the PVS is believed to be pulsations from arterial walls, driven by cardiac contractions. These pulsations create pressure gradients that help propel CSF along the PVS, facilitating the removal of waste products. The PVS is a major component of several transport pathways with the two most significant further described below. [6]

### 1.2.1 Glymphatic System

The glymphatic system is a macroscopic transport system in the brain that relies on the communication of CSF and ISF through the PVS. In some respects it is functionally analogous to the lymphatic system, having a crucial role in both waste clearance and transport of immune cells and signaling molecules. The cycle begins with CSF being driven into the PVS by a combination of arterial pulses, respiration and relative pressure gradients. Exchange between the PVS and brain parenchyma is regulated via AQP4 channels located in the endfeet of astrocytes. These channels facilitate the movement of water and solutes, enabling both passive and active transport mechanisms. The influx of CSF from periarterial spaces drives ISF flow into the perivenous tissue. The ISF then continues along the perivenous space until it drains to the cervical lymphatic system. [4, 1]

The glymphatic system is characterized by a circadian rhythm, with its flow rate being significantly lower during wakefulness, approximately 10% of the rate observed during sleep.[7] This reduced flow during wakefulness persists regardless of whether sleep is natural or pharmacologically induced. Current evidence suggests that sleep-associated changes, including increased interstitial volume, facilitate more efficient fluid exchange. [8] Additionally, studies have demonstrated that the active glymphatic state observed during sleep can be induced in awake mice by blocking norepinephrine receptors. [7, 8]

### 1.2.2 Intramural Periarterial Drainage

An alternative pathway for transport through PVS is the IPAD. This pathway utilizes the basement membranes, which are laminar sheaths of extracellular matrix surrounding arterial walls, to facilitate the movement of interstitial fluid and solutes. These basement membranes are at the edge of the blood vessel so for periarterial spaces it would be more appropriate to say that the PVS exists between astrocytic endfeet and basement membranes. This drainage mechanism is more closely linked to the transport of beta-amyloid, a waste product linked to several disorders. [1]

### 1.2.3 Pathology

The most commonly used indicator for PVS abnormality is enlarged diameter. However, enlarged spaces occur across all age groups, in healthy and pathological subjects. However, there is a significant correlation between PVS enlargement and aging. [9] This correlation is also seen in neurodegenerative disorders like Alzheimer's and Parkinson's disease. [10] Most of these changes are straightforward, the PVS surrounds the blood vessels so the age related factors that cause vascular changes will also cause changes in the PVS. Reduced arterial compliance reduces the pulsatile force which in turn reduces the PVS diffusivity. Vascular basement membranes thicken reducing the capabilities of the IPAD. The AQP4 polarization is impacted, limiting active transport. Finally, the blood-brain barrier breaking down can cause vascular waste components to build up within the PVS, further exacerbated by the reduced drainage ability. Critically, this reduced flow rate causes buildup of neurotoxic waste such as beta-amyloid or tau-protein. Both of these waste products are linked with neurodegenerative disorders. The direction of causality is unknown. It is possible that the reduced glymphatic function causes the pathology and the detected buildup is merely an indicator. Alternatively, the increased presence of the waste products cause both the pathology and a reduction in PVS flow. Regardless, enlargement of the PVS can act as a biomarker of pathology, possibly allowing early detection or new avenues of treatment. [1]

## 1.3 State-of-Art

### 1.3.1 Contrasts

PVS is typically imaged using T2w MRI as the high fluid content within the PVS results in a bright signal. However, free floating water outside of the PVS due to pathologies like edema or lacunae has a similar signal intensity. A T1w image can help differentiate these but has worse PVS contrast. An alternative contrast proposed by Sepehrband et al is the EPC. The EPC is obtained by applying a non-local means filter to preprocessed and registered T1w and T2w images before dividing T1w by T2w. This resulting image makes use of both modalities to differentiate the PVS from other sources of free water and improve the contrast between PVS and surrounding tissues. Visibly PVS is much easier to spot and smaller spaces can be detected.[11]

Although PVS surrounds both arterioles and venules there is significant evidence that the majority of visible PVS on these contrasts is periarterial rather than perivenous. [12, 13] There are several possible explanations for this. Perivenous spaces are smaller and likely have a different fluid composition. This could result in a lower relative signal intensity to surrounding parenchyma. Additionally, it has been shown that enlargement of the PVS occurs more frequently with periarterial spaces, which may be more prone to dilation due to vascular aging or pathology. These factors contribute to the greater prominence of periarterial PVS in imaging studies and may affect their visualization with different imaging contrasts. [12, 11, 13]

### 1.3.2 Gadolinium-Based Contrast Agents

Another option for quantitative imaging of the PVS is the use of Gadolinium-based contrast agents. These agents enhance T1w signals and can be used with dynamic contrast enhanced MRI to obtain a time series. The GDBA, once administered to a peripheral vein, arrives in the subarachnoid space. From here they follow the typical glymphatic pathway, being forced into the periarterial space with the CSF before perfusing the parenchyma. Accounting for the pharmacokinetic properties of the agent, the rate of diffusion within the PVS can be estimated. Although this method does not directly visualize the PVS it can allow for a global model of glymphatic function. Such a model is easily compared intra- and inter-subject suggesting suitability for research comparing glymphatic function with many pathologies. However, due to the invasive nature of the administration and concerns about potential toxicity, its clinical utility is limited, and it is not suitable for large-scale imaging studies. [14, 15]

### 1.3.3 Visual Scoring

Visual scoring has been the standard clinical practice for several years. There are two main scoring approaches for PVS. The first takes any visible vessels as enlarged, this is simply counting visible PVS in a region with a grade based on the number observed. The second takes into account the diameter of the vessels, either weighting the rating based on size or only considering a vessel enlarged if it is over a specific diameter. Typically several regions are scored independently, for example the basal ganglia and the centrum semiovale. The main benefit of visual scoring for PVS is it can be performed on both T1w and T2w images with no specific acquisition parameters. However, this process is very time consuming, lacks scoring granularity, and can be very ROI dependent. [11]

### 1.3.4 DTI-ALPS

One of the most well known methods for estimating diffusivity of the perivascular space is the DTI-ALPS Index. This is an ROI based method which makes strong assumptions about the orientation of PVS relative to white matter in several regions of the brain. Based on this assumption it is then possible to estimate PVS behavior based on relative fractional anisotropy without having to segment the tissues. Following the Figure 1.2 below, it begins with a simplified model of cerebral vasculature. Waste must reach the surface and it tends to travel along the red line through the medullary vessels. Looking at the DWI overlay you can see white matter orientations, one in each circled area. Along these three ROI the assumption is that the angles between WM in the projection area, WM in the association area, and the PVS are orthogonal. This relationship allows for a simple ratio based on the fractional anisotropy of radial diffusivities for both WM orientations. If this assumption holds, then the ratio between the radial diffusivity oriented along the PVS versus orthogonal to the PVS should be a measure of diffusivity along that space. [3, 16]

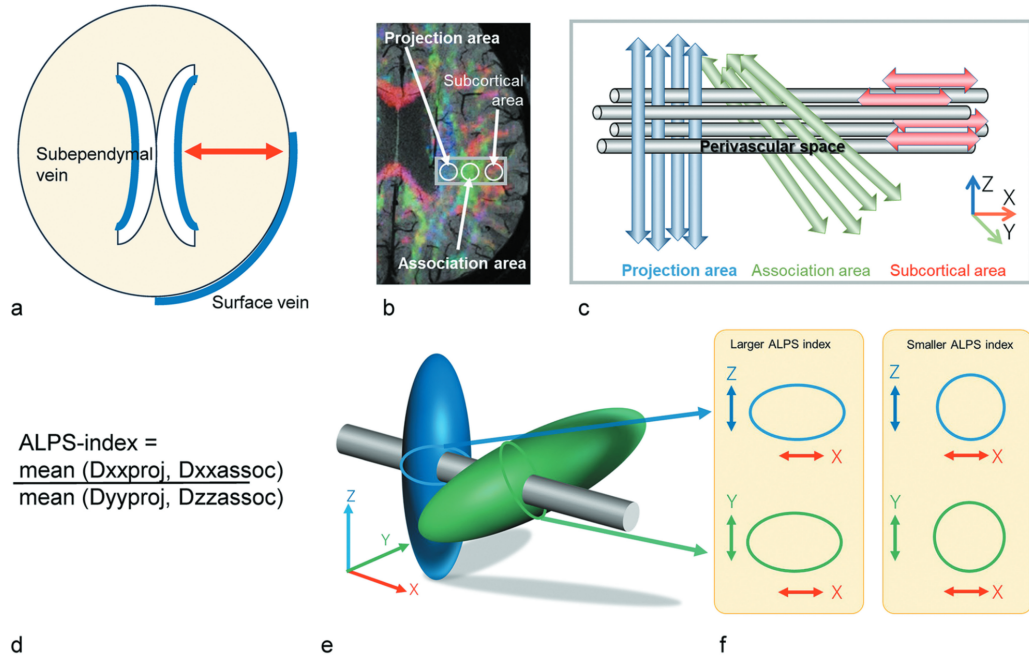


**FIGURE 1.2: DTI-ALPS Background and Methodology.** A: Simplified cerebral vasculature model. B: DWI overlaying SWI. C: Orientation model. D: ALPS-Index equation. E: Diffusion tensor visualization. F: Fractional anisotropy comparison. [16]

Although this appears to be an effective way to measure glymphatic function a recent study by the same author reevaluates his method to highlight some of the inherent limitations. The DTI-ALPS Index is ultimately a local model, only measuring diffusivity in a small region. Pathology in this region such as edema or lesions will have exaggerated effects on the index assigned to the patient. Further, the loose positioning of the ROI means that the method is dependent on expert placement and it would be challenging to remain consistent across large studies. It is also quite difficult to place an ROI that wide in those areas without encountering partial volume effects from nearby WM tracts. There is also evidence that the orthogonality assumption does not hold for conditions with brain deformation. The most significant downside is that there is insufficient evidence that glymphatic function in one region is representative of function in the rest of the brain. A global model would be required to resolve this issue. [16]

## 1.4 Datasets

As with any imaging study the signal-to-noise ratio and resolution are two of the most important considerations. These are the limiting factors to what kind of tissue you can examine and how meaningful your results can be. Clinical MRI imaging tends to produce structural resolutions around 1mm and diffusion from 2–3mm. Since the majority of PVS are smaller than 1mm clinical imaging is clearly insufficient. Further, the small scale of the vessel and its diffusion signal necessitate more complex diffusion acquisition. Clinical diffusion data is typically 3T and tends to use fewer measurement angles and b-values. SNR is proportional to field strength so this study will use 7T DWI.

### 1.4.1 Human Connectome Project

The majority of this study was performed on the Young Adult Dataset from the Human Connectome project. It is one of the most comprehensive high resolution neuro-oriented datasets available, combining structural, diffusion, resting fMRI and task fMRI data of 1200 subjects from 22-35 years old. The novelty of the HCP was creating a thorough acquisition and preprocessing pipeline for high resolution multi modal MRI data. This has become the standard for high resolution neuro-imaging. The structural resolution of this dataset is 0.7mm isotropic, nearing the hardware limitations for full brain scans. The diffusion data was taken at 7T with an isotropic resolution of 1.25mm. Sampled with 3 shells ( $b1000, b2000, b3000 \text{ s/mm}^2$ ) at 90 directions each. The importance of multiple shells and HARDI protocols will be further explained in the diffusion chapter. [17]

### 1.4.2 Natural Scenes Dataset

The natural scenes dataset is primarily aimed at capturing fMRI data from 8 subjects. It is limited to only 8 subjects due to its extensive acquisition procedures. This dataset was included in this study for its unusual variety of high resolution contrasts, including 7T susceptibility weighted imaging, 7T high-res T2, and 3T angiography. Unfortunately, the diffusion data was only 3T with a 1.5mm resolution so this dataset is only useful for the segmentation portion. The T1w and T2w images have a resolution of 0.8mm which is close enough to the HCP resolution for meaningful comparison. [18]

# Chapter 2

## Structural Analysis of PVS

This chapter begins with an overview of the relevant filtering methods, followed by a brief introduction to Susceptibility-Weighted Imaging (SWI). Next, the two implemented segmentation methods are explained in detail. The validation process is then covered, including the visual scoring criteria and the use of SWI. The chapter concludes with a discussion of the methods considered for deriving PVS orientation based on the validated segmentation.

### 2.1 Background

#### 2.1.1 Vessel Detection: Hessian and Frangi Filter

Vessel detection in medical imaging requires methods capable of distinguishing tubular structures, such as blood vessels or fiber bundles, from surrounding tissues. One of the most effective approaches for this task involves the use of the Hessian matrix and the Frangi Vesselness Filter. The Hessian matrix is a second-order derivative matrix that captures the local curvature of an image, which is essential for identifying the geometric properties of structures. Mathematically, the Hessian matrix  $H$  at each voxel is defined as the matrix of second-order partial derivatives of the image intensity function  $I(x, y, z)$ , as shown below:

$$H = \begin{bmatrix} \frac{\partial^2 I}{\partial x^2} & \frac{\partial^2 I}{\partial x \partial y} & \frac{\partial^2 I}{\partial x \partial z} \\ \frac{\partial^2 I}{\partial y \partial x} & \frac{\partial^2 I}{\partial y^2} & \frac{\partial^2 I}{\partial y \partial z} \\ \frac{\partial^2 I}{\partial z \partial x} & \frac{\partial^2 I}{\partial z \partial y} & \frac{\partial^2 I}{\partial z^2} \end{bmatrix}$$

The eigenvalues  $\lambda_1, \lambda_2, \lambda_3$  of this matrix describe the principal curvatures of the image at each point, where  $\lambda_1$  typically represents the smallest eigenvalue, aligned with the direction of the vessel (i.e., the tubular structure). The larger eigenvalues,  $\lambda_2$  and  $\lambda_3$ , correspond to the perpendicular directions. In the context of vessel detection, a tubular structure is characterized by large curvature along one axis and smaller or negative curvatures along the perpendicular axes.

The Gaussian filter is commonly applied before computing the Hessian matrix to stabilize the derivative calculations and reduce the impact of noise. The Gaussian filter smooths the image at different scales, effectively reducing high-frequency noise and enhancing the relevant structures. The filter applies a weighted average to neighboring pixels, with the weights determined by the Gaussian function. The scale of the Gaussian filter, represented by the parameter  $\sigma$ , controls the level of smoothing: larger values smooth the image over a broader area, capturing coarser features, while smaller values retain finer details. The smoothed image helps in computing the second-order derivatives more reliably, ensuring that the Hessian matrix represents the true curvature of structures. [19]

The Frangi Vesselness Filter [19] is a specialized application of the Hessian matrix that can detect and enhance vessel-like structures in an image. It combines the eigenvalues of the Hessian matrix to calculate a vesselness score, which quantifies the likelihood of each voxel belonging to a vessel. The vesselness function is defined as:

$$V(x, y, z) = \begin{cases} 0, & \text{if } \lambda_2 > 0 \text{ or } \lambda_3 > 0 \\ \left(1 - \exp\left(-\frac{R_a^2}{2\alpha^2}\right)\right) \exp\left(-\frac{R_b^2}{2\beta^2}\right) \left(1 - \exp\left(-\frac{S^2}{2c^2}\right)\right) & \text{otherwise} \end{cases} \quad (2.1)$$

Here:

- $R_a = \frac{|\lambda_2|}{|\lambda_3|}$  captures the relative contrast between the two largest eigenvalues,
- $R_b = \frac{|\lambda_1|}{\sqrt{|\lambda_2 \lambda_3|}}$  measures the blobness versus tubularness
- $S = \sqrt{\lambda_1^2 + \lambda_2^2 + \lambda_3^2}$  accounts for noise suppression.

The parameters  $\alpha$ ,  $\beta$ , and  $c$  control the sensitivity of the filter:

- $\alpha$  adjusts the suppression of plate-like structures,
- $\beta$  enhances the tubular appearance,
- $c$  regulates the overall vesselness response and suppresses noise.

This formulation ensures that regions with large positive eigenvalues (non-tubular regions) are suppressed, while vessel-like regions with one large eigenvalue and two smaller ones are enhanced.

The scale parameters play a critical role in adjusting the sensitivity to different vessel types. By changing these parameters, the filter adapts to detect vessels of varying sizes and shapes, enabling multiscale vessel detection. A larger value for  $\sigma$  enhances the detection of larger vessels, while smaller values focus on finer details, allowing for comprehensive vessel enhancement across multiple scales. [19]

### 2.1.2 Susceptibility Weighted Imaging

Susceptibility Weighted Imaging (SWI) is a specialized MRI technique that enhances tissue contrast based on differences in magnetic susceptibility, a material property that describes the degree to which a substance becomes magnetized when placed in a magnetic field. Magnetic susceptibility varies across different tissues due to differences in their composition, such as the presence of paramagnetic (iron, deoxygenated blood) and diamagnetic (calcium, myelin) substances. These variations in susceptibility cause local distortions in the magnetic field, which result in changes in the phase of the MRI signal. While these phase shifts are typically considered artifacts in most imaging sequences, SWI leverages them to generate detailed images of these susceptibility differences [20].

The acquired phase information reflects the local magnetic field variations caused by the susceptibility of nearby tissues. This phase image is high pass filtered and unwrapped to create the phase mask. Phase wrapping occurs when phase shifts exceed the range from  $-\pi$  to  $\pi$ , causing the phase to "wrap around". Phase unwrapping algorithms correct these discontinuities by ensuring a continuous phase representation. The magnitude image, which provides overall tissue signal intensity, is then modulated by this phase mask to highlight areas of interest, such as veins or microbleeds, which are otherwise difficult to visualize in conventional MRI sequences. Once the phase data is acquired, it is typically subjected to phase unwrapping. [20]

Quantitative Susceptibility Mapping (QSM) is similar to SWI but quantifies tissue magnetic susceptibility using only the phase data. QSM provides quantitative measurements of magnetic susceptibility, allowing precise differentiation between paramagnetic substances (e.g., iron) and diamagnetic substances (e.g., calcium). [21] The relationship between the phase shift ( $\phi$ ), local magnetic field variations ( $\Delta B$ ), and tissue susceptibility ( $\chi$ ) is governed by the following equations:

$$\phi = \gamma \Delta B T_e \quad \Delta B = D \cdot \chi \quad \chi = D^{-1} \Delta B$$

Here,  $\gamma$  is the gyromagnetic ratio,  $T_e$  is the echo time, and  $D$  is the dipole kernel that relates susceptibility to the magnetic field inhomogeneities. The inversion of  $D$  to compute  $\chi$  is ill-posed, requiring regularization techniques to reduce noise and improve stability.

## 2.2 Segmentation

### 2.2.1 Enhanced Perivascular Contrast

The structural HCP data has already undergone preprocessing as part of the HCP pipeline, which includes correction for gradient nonlinearity, registration, and alignment with native space using anterior commissure-posterior commissure (AC-PC) alignment. Following this, adaptive non-local means filtering is applied to the T1w and T2w images using the `VolumeFilterNLM` function from the Quantitative Imaging Toolkit (QIT) [22, 23]. The filtering process uses Rician noise and a patch size of 1, as outlined in [11].

Occasionally, the filtered images contained null values, which were primarily located within the ventricles or near the meninges. These areas were considered unlikely to affect subsequent analyses, so the nullified values were replaced with corresponding values from the unfiltered images.

The final EPC image was created by dividing the processed T1w and T2w images ( $T1w / T2w$ ). To improve visualization, the T1w image was divided by the minimum of 10 and the T2w signal in each voxel. Although this additional step is not explicitly mentioned in the original work, it ensures that intensity values remain within a reasonable range, particularly in regions with high-intensity signals, such as unstripped bone.

### 2.2.2 Heuristic Frangi Filter for the EPC

The original study on EPC also introduced a heuristic filter for segmenting the PVS to enable automated quantification, with this studies implementation discussed below. [11]

First, masking was performed using Mrtrix3's `5ttgen` FSL on T1-weighted images, restricting the segmentation to white matter regions. The original study, however, utilized n-tissue parcellation from the Advanced Normalization Tools (ANTS) software package [24], which also included the basal ganglia. This difference in parcellation had little effect on the final PVS segmentation results.

The Frangi filter, implemented using QIT's `VolumeFilterFrangi` [22, 19], was used to calculate the vesselness score. The score was normalized and thresholded according to the following equations:

$$\hat{V} = \frac{V - \min(V)}{\text{IQR}(V)}$$

$$P(s) = \begin{cases} 1 & \text{if } \hat{V} \geq t \\ 0 & \text{otherwise} \end{cases}$$

Here,  $\hat{V}$  represents the normalized vesselness score, and  $t$  is the threshold applied to produce the binary mask  $P$ . While the original study recommended a threshold of  $t = 1.5$  for EPC segmentation [11], this implementation performed better with  $t = 0.5$ . The discrepancy was later attributed to an implementation error.

Sepehrband et al. [11] recommended default parameters  $\alpha = 0.5$ ,  $\beta = 0.5$ , and  $c = 300$ , based on the original Frangi filter. These parameters were adopted in this study. Additionally, it was suggested to normalize  $c$  by setting it to half the maximum Hessian norm. This adjustment enables the filter to adapt dynamically to the vesselness characteristics of the image, allowing for sensitivity to large curvatures in brains with many enlarged PVSs, and vice versa. In contrast, using a fixed value for  $c$ , as implemented here, resulted in a more rigid filter that struggled to accurately capture abnormal PVS presentations.

Despite the identified implementation error, recalibrating the threshold yielded performance comparable to that reported in the original study for the majority of images.

However, the heuristic nature of the Frangi filter presents inherent limitations. The PVS exhibits significant heterogeneity, varying across individuals and brain regions. This variability challenges the fixed application of the filter, as it often fails to generalize across datasets with differing PVS characteristics. To address these limitations, an automated neural network model was subsequently developed and is discussed in the following section.

### 2.2.3 Weakly-Supervised Perivascular Space Segmentation

The Weakly-Supervised Perivascular Space Segmentation (WPSS) [25] is an automated approach for segmenting PVS. Implementing supervised learning for PVS segmentation presents significant challenges due to the time-consuming nature of manual segmentation, which makes creating large datasets impractical.

To address this, the training data is initially generated through heuristic segmentation using the Frangi filter. This data is then manually quality-controlled to ensure its accuracy. While this provides a foundation for model training, it is insufficient for developing a fully labeled, supervised learning dataset. As a result, the model is trained using weak supervision. In weakly-supervised learning, the model is provided with limited or noisy annotations rather than precise ground truth. Through the use of weak signals, the model identifies underlying patterns, enabling it to generalize beyond the training data and perform effectively with fewer annotations.

This particular model was chosen because it is trained on the EPC derived from the HCP data. Pre-trained weights for EPC segmentation were made available upon request, and these weights were utilized to generate the segmentations. The following sections detail the significance of each model component. For additional information on training and regularization, please refer to [25].

**Frangi CNN:** This portion of the model implements a rule-based Frangi filter with parameters  $\alpha$ ,  $\beta$ , and  $c$ , which are tuned during training. Three different Gaussian kernels are applied at varying scales, with the scale parameter being a trained value. The Frangi CNN computes vesselness using the measures  $R_a$ ,  $R_b$ , and  $S$ , as defined in equation 2.1. The network outputs a three-channel PVS probability map, with each channel corresponding to the vesselness derived from a different kernel.

**UNET CNN:** In parallel with the Frangi CNN, the EPC image is also provided as input to a UNET CNN. This network captures broader physiological patterns, which helps to refine the segmentation process. By learning these global patterns, the UNET improves the model’s ability to distinguish between PVS regions and surrounding tissues. It outputs a two-channel probability map, where one channel represents the likelihood of a voxel being PVS and the other represents the likelihood of it being non-PVS.

**CRF RNN:** The outputs from the previous networks—a three-channel PVS probability map from the Frangi CNN and a two-channel probability map from the UNET—are combined using a Conditional Random Field Recurrent Neural Network (CRF RNN). The CRF RNN refines the segmentation by enforcing spatial consistency and leveraging contextual dependencies between neighboring pixels. This allows the model to correct any inconsistencies in the segmentation, enhancing the precision of boundary delineation and reducing noise.

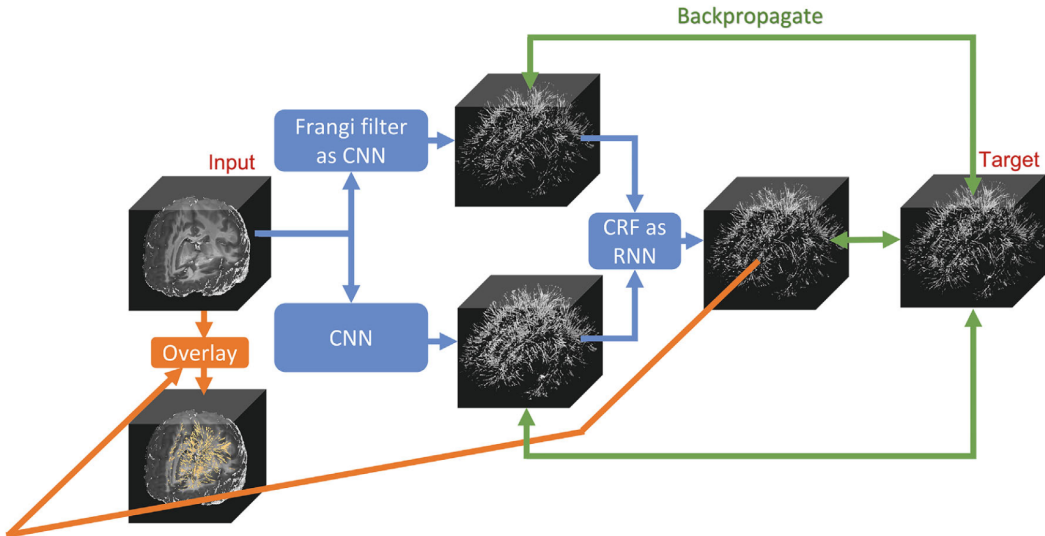


FIGURE 2.1: **Network Architecture of WPSS.** The blue lines indicate the input path of the EPC image, followed by the three- and two-channel network outputs into the CRF RNN. The green lines represent the separate backpropagation from the target to all three networks. Backpropagation is applied to each component separately to reduce training complexity and improve stability. [25]

## 2.3 Validation

### 2.3.1 Visual Scoring

In order to perform a quantitative assessment of segmentation performance a visual scoring procedure was devised and implemented as explained in detail below. Three segmentation methods were scored for each image: EPC Frangi with the recommended threshold, EPC Frangi with a calibrated threshold, and WPSS.

#### Criteria

The scoring process begins by assigning a base score, ranging from one to five, based on the visible accuracy of the segmentation relative to the expected accuracy. The expected accuracy is the ideal segmentation outcome, given the quality of the available imaging and the segmentation methods used. There are several regions with visible PVS that are unrealistic to expect a segmentation of such as the juxtaparaventricular PVS. In this region the contrast and SNR appears lower and it would be very challenging to see the PVS. However, these spaces are also mostly in plane on an axial slice so they are easier to follow visually. In these areas it is possible to see the overall path that a PVS is taking even with low SNR and large gaps. However, neither segmentation methods explicitly track PVS direction so it is unrealistic to expect these regions to be segmented. This is the most subjective aspect of the scoring, the scorer must decide what PVS should reasonably be segmented by the methods given the information available to them.

Once this base score is established, it is then penalized based on common segmentation flaws that often arise during PVS segmentation. For each of these flaws, a single point is deducted from the base score. These flaws are detailed below:

1. **Failure to capture large PVS:** A penalty is applied when large PVS are not detected. This can occur due to the limitations of the Frangi vesselness filter used in both segmentation methods. The filter's performance is dependent on the sigma values chosen, which dictate the range of vessel sizes it can detect. If a PVS surpasses the upper limit of this range, it will be overlooked in the final segmentation mask. To address this, an ideal segmentation tool should be sensitive to vessels of various sizes, with variable thresholding allowing the capture of a broader range of scales.
2. **Excessive sensitivity to noise in the pons and medulla oblongata:** In some EPC images, there appears to be higher noise in these regions, which can be incorrectly marked as PVS. Subjectively, this increased noise appears to be correlated with an increase in PVS-like noise in other regions of the brain. This region acts as a litmus test for the segmentation's ability to deal with noisier contrasts.

3. **Segmentation errors around the lenticulostriate arteries:** A penalty is applied when PVS is inaccurately segmented in and around the lenticulostriate arteries. As described in Chapter 1, these arteries contain PVS that are typically larger than normal, symmetric, and exhibit minimal variation across subjects. These spaces are consistently visible in all subjects and do not show significant enlargement in patients with more pronounced PVS. Due to their distinctiveness, it is reasonable to expect a segmentation tool to avoid incorrectly classifying these areas as part of the PVS. Therefore, errors in this region are penalized.

## Results

Visual scoring of perivascular space (PVS) segmentation was conducted on a cohort of 30 subjects. The recommended threshold for the heuristic segmentation performed poorly, achieving an average score of 1.45. In comparison, the recalibrated heuristic segmentation showed marked improvement, with an average score of 2.9. The WPSS method consistently outperformed both heuristic approaches, achieving a base score of 5 on most images and an adjusted average of 4.4 when accounting for penalties.

The heuristic methods generally produced lower base scores than WPSS, with notable limitations in capturing juxta-cortical regions and PVS near the centrum semiovale. They were frequently penalized for failing to detect large PVS and for erroneously segmenting lenticulostriate arteries.

In contrast, WPSS demonstrated better segmentation consistency but was similarly susceptible to noise, particularly in regions around the medulla oblongata and the third ventricle. Despite its advantages, WPSS, like the heuristic methods, struggled to detect extremely enlarged PVS, underscoring a shared limitation in these algorithms.

Both approaches also exhibited reduced performance on images with atypical white matter (WM) contrast, where excessively bright or dark WM relative to surrounding tissue posed challenges for accurate segmentation. Detailed results of the visual scoring, along with subject-specific notes, are provided in the Appendix.

### 2.3.2 Susceptibility Weighted Imaging

The venograms generated by SWI have a much higher resolution than the structural contrasts from the HCP data and in theory, due to their reliance on phase over magnitude, a higher SNR. [20] Because of this, it was hypothesized that by applying a thresholded vesselness filter to the venogram, a mask of the venous vasculature could be created that significantly correlates with the perivenous spaces. In this way a form of ground truth could be generated for the majority of perivenous spaces. This cross correlation of this mask with a PVS segmentation looking only for amount of true positive voxels could provide an automated method to assessing PVS segmentation based on the rate of perivenous segmentation.

The HCP data does not include SWI so another dataset, Natural Scenes was used. This has 0.8mm structural data but otherwise uses the same acquisition and preprocessing pipeline as HCP data. The EPC contrasts were generated from interpolated T1w and T2w. The segmentation performed with only slightly reduced performance. This was to be expected due to the lower native resolution. When this EPC and segmentation was compared to the venogram there was little to no correlation between visible venous vasculature and the segmentation. Furthermore, the performance of the vesselness thresholding to segment the venogram was too poor for meaningful comparison, only the veins and larger venules were segmented. However, as shown in figure 2.2, there was visible overlap between some of the high intensity areas of the venogram. There was also several PVS visible on the EPC with gaps that appeared to be bridged by high intensity vessels on the venogram.

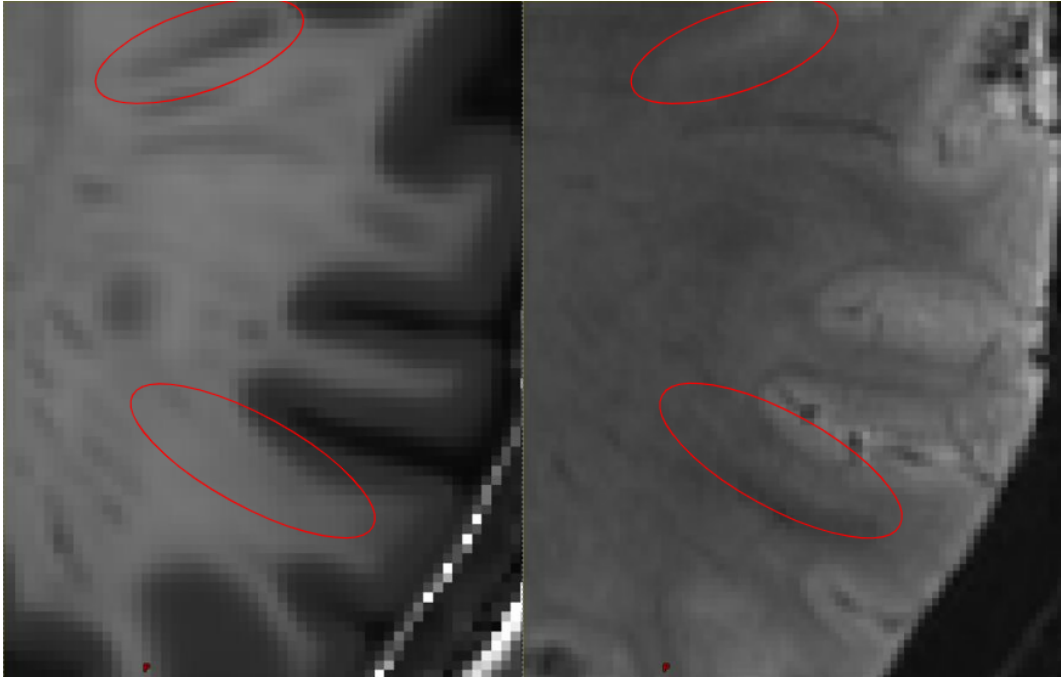


FIGURE 2.2: **Comparison of EPC with SWI.** EPC-left, SWI-right. Circled in red are notable visible PVS. The top circle demonstrates a large PVS with a corresponding high intensity SWI signal, suggesting it is periarterial. The bottom circle demonstrates the start and end of a PVS vessel on the EPC which is entirely visible on the SWI.

## 2.4 Capturing Orientation

Once the segmentation is available, the next step is to estimate the voxel-wise orientation. Orientation estimation methods must carefully balance two key factors: the reliability of the segmentation and physiological assumptions about the perivascular space (PVS). For example, it is reasonable to assume that PVS vessels are continuous and do not abruptly terminate. However, the segmentation will always have gaps or sharp changes in width due to noise or insufficient resolution.

This understanding influences the choice of method for orientation estimation, where one must consider how much trust is placed in the segmentation versus incorporating assumptions about the inherent structure of the vessels. The methods used for orientation estimation involve trade-offs between capturing local geometric details and maintaining computational efficiency. The first approach attempted was vector estimation via Principal Component Analysis (PCA), which had several limitations discussed later. Subsequently, a Hessian-based method was implemented, which overcame the shortcomings of PCA and was ultimately used for the final vector field estimation in the following chapters.

### 2.4.1 Principal Component Analysis (PCA)

Principal Component Analysis (PCA) begins by extracting an  $n \times n \times n$  size kernel around each voxel. The kernel size can be adjusted to control the balance between local and global curvature of the vessel. A smaller kernel emphasizes local structure, capturing finer geometric details, while a larger kernel captures a broader context of the vessel's geometry. PCA is a simple and computationally inexpensive method that analyzes the distribution of points in the local neighborhood and estimates the direction of maximum variance in that region. The core of PCA lies in analyzing the covariance of the spatial distribution of points within the neighborhood. The covariance matrix,  $\Sigma$ , is calculated as:

$$\Sigma = \frac{1}{N} \sum_{i=1}^N (\mathbf{x}_i - \bar{\mathbf{x}})(\mathbf{x}_i - \bar{\mathbf{x}})^T$$

Where:

- $N$  is the number of points in the neighborhood,
- $\mathbf{x}_i$  represents the coordinates of the  $i$ -th point,
- $\bar{\mathbf{x}}$  is the mean of the coordinates in the neighborhood.

The covariance matrix captures the variance of points in each direction, and PCA identifies the eigenvectors corresponding to the largest eigenvalues of this matrix. The eigenvector with the largest eigenvalue represents the direction of maximum variance, which is then taken as the orientation of the vessel at that voxel. However, PCA has limitations in capturing local curvature or non-linear vessel structures. Specifically, PCA tends to represent the overall direction of the vessel in the kernel without accounting for localized bending or branching. While this makes it effective for relatively straight vessels, it becomes less accurate in regions with sharp curvatures or more complex geometries. These limitations prompted the exploration of the Hessian method, which more effectively captures local curvature and complex vessel geometries.

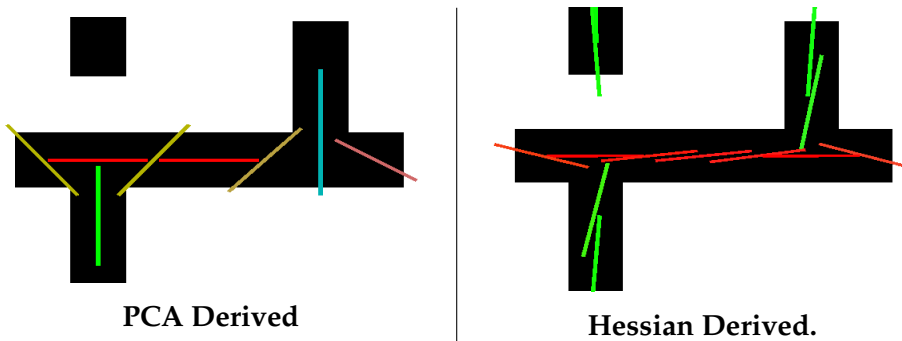
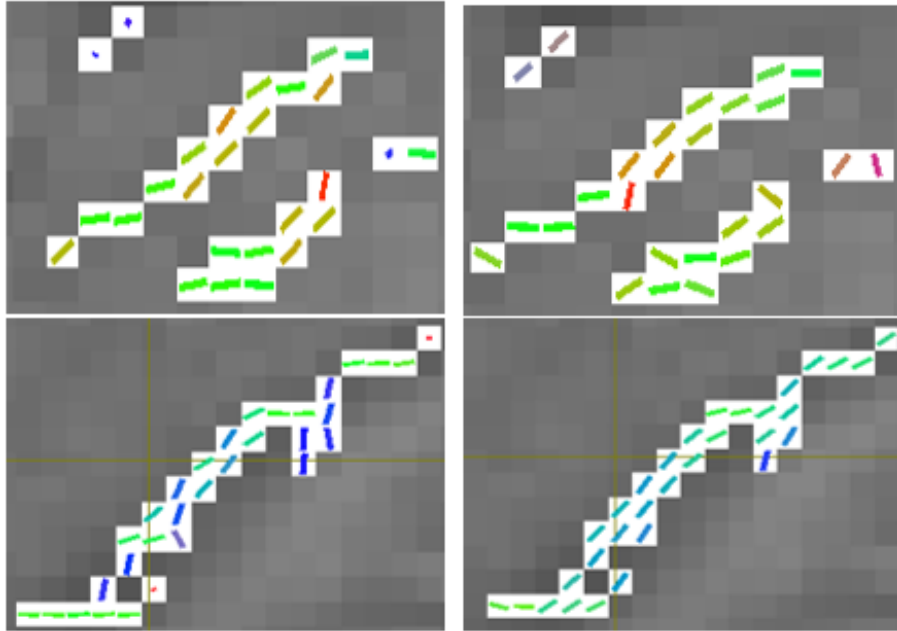


FIGURE 2.3: PCA vs Hessian Orientation Phantoms. This phantom highlights each models behavior under rapid changes of direction and their ability to capture the global direction of the vessel.

### 2.4.2 Hessian Maximum Curvature

To overcome PCA's limitations in capturing local curvature, the Hessian matrix method was employed. This technique uses second-order derivatives combined with Gaussian smoothing to stabilize the computations and reduce noise. The smoothing parameter, sigma, directly influences the level of detail captured: a larger sigma smooths out the orientation, while a smaller sigma retains finer vessel details. This method provides more accurate orientation estimates, especially in regions with sharp turns or branching. As a result, the Hessian method was selected for final orientation estimation, offering superior accuracy in capturing vessel geometry.

In practice, when applying Hessian filters to vessels, most perivascular space (PVS) segmentations are approximately 1–3 voxels wide. This small range makes the vessel width a negligible factor in optimizing the Gaussian smoothing. Instead, the smoothing factor influences how far along a vessel the algorithm looks. As demonstrated in 2.4, using a sigma value that is too low or too high significantly affects the results. For the PVS segmentation the optimal Gaussian smoothing was determined to be approximately 0.7 voxels. This results in an effective max range of 2.1 voxels ( $3 \times \sigma$ ).



**FIGURE 2.4: Hessian-based PVS Orientation.** On the left, the orientation derived from the Hessian method uses a Gaussian sigma of 0.5. This lower smoothing captures sharp changes in angle, leading to abrupt shifts in direction. On the right, a higher sigma of 1 is applied, which smooths the orientation field significantly. While this improves the overall representation, it introduces artifacts, with nearby vessels causing some abrupt directional changes. The higher sigma field on the right offers a smoother overall orientation but at the cost of reduced sensitivity to sudden shifts that may be physiologically relevant.

## Chapter 3

# Modelling PVS Diffusion

This chapter will begin with an introduction to the acquisition and modelling techniques used in diffusion weighted imaging. These techniques will form the basis for the PVS diffusivity metrics including the incorporation of the structural segmentation and its vector field. Finally, the diffusivity metrics will be evaluated on synthetic data simulating the behavior of each model under a range of conditions.

### 3.1 Background

The brain comprises bundled nerves, glial tissue, vasculature, cerebrospinal fluid, connective tissues like the meninges, and supportive frameworks such as the perivascular spaces. Together, these form a network of fluid-filled spaces enveloped by intricate barriers. While the structural imaging methods discussed in the previous chapter offer valuable contrast based on the composition of these tissues, they are limited in their ability to delineate the geometry and continuity of the barriers within and between tissues.

#### 3.1.1 Diffusion Weighted Imaging

Diffusion-Weighted Imaging (DWI) differs from conventional structural MRI by focusing on the displacement of water molecules to reveal tissue microstructure. Water molecules in biological tissues undergo Brownian motion, leading to random displacements with a Gaussian distribution in unrestricted environments. Over longer timescales, the zero-mean displacement suggests that molecules will return to their original position. However, the timescales in DWI are typically too short for this to occur, leading to fluctuating signal changes rather than a stationary signal. Additionally, water diffusion in the brain is not completely free. When water molecules encounter barriers such as cell membranes, axonal bundles, or other structural elements, their movement is either hindered or restricted. Hindered diffusion refers to partial obstruction, such as radial diffusion through white matter tracts, while restricted diffusion occurs when water is completely confined within boundaries, resulting in an isotropic reduction in diffusivity. [26]

### Measurement of Diffusivity

To measure molecular diffusivity, the Pulsed Gradient Spin Echo (PGSE) sequence is employed. This sequence involves:

1. **90-degree excitation pulse:** Aligns proton spins into the transverse plane.
2. **Dephasing gradient pulse:** Creates spatially dependent phase shifts based on molecular positions.
3. **180-degree refocusing pulse:** Reverses the phase evolution.
4. **Second gradient pulse:** Attempts to rephase spins.

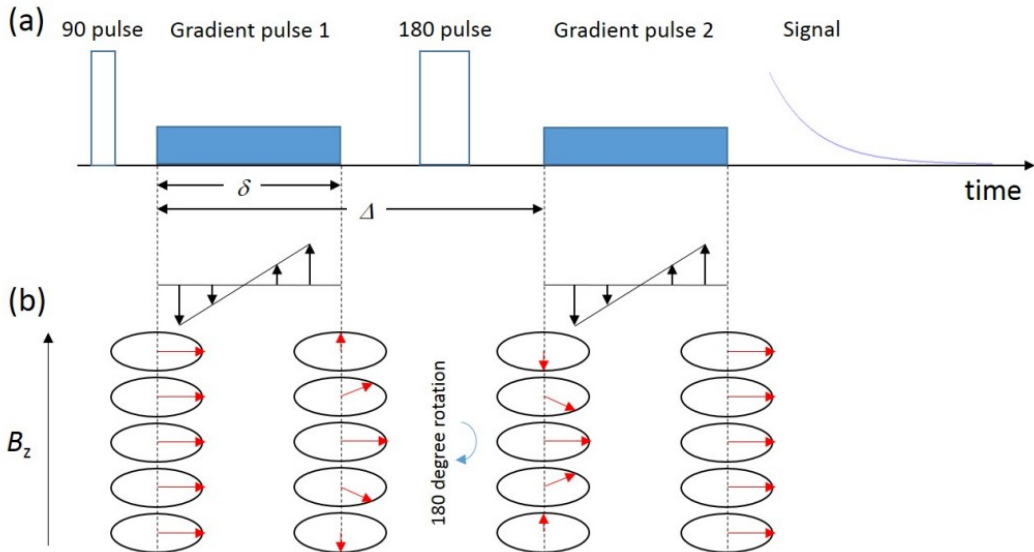


FIGURE 3.1: A.) Schematic representation of PGSE sequence. B.) Phase evolution of spins along the gradient direction. [27]

Molecules that remain stationary are perfectly rephased, while those that move relative to gradient direction result in signal attenuation. The degree of attenuation correlates with diffusivity, providing a quantitative measure of water movement. [26]

### b-Value and Diffusion Gradients

In practice, this simplification is not entirely accurate. The movement of water molecules is influenced by other factors, such as perfusion—the flow of blood through tissues—which can contribute to signal changes that are not purely related to diffusion. To account for this and better quantify the contribution of diffusion to the signal, a metric called the b-value is introduced. The b-value characterizes the strength and timing of the applied diffusion-weighting gradients, and it helps separate the effects of diffusion from other influences, like perfusion, allowing for a more accurate measurement of molecular diffusivity. [26]

The b-value quantifies the strength and timing of diffusion-weighting gradients, encapsulated in the equation:

$$b = \gamma^2 G^2 \delta^2 \left( \Delta - \frac{\delta}{3} \right)$$

where:

- $\gamma$  : gyromagnetic ratio,
- $G$  : gradient strength,
- $\delta$  : duration of the diffusion gradient pulse,
- $\Delta$  : time between gradient pulses.

Higher b-values increase sensitivity to restricted diffusion, allowing better characterization of microstructural barriers. However, they also reduce SNR due to greater signal attenuation. Conversely, lower b-values have higher SNR and are more sensitive to hindered diffusion and perfusion effects, providing complementary information.

### Signal Attenuation and ADC

The relationship between the diffusion-weighted signal and diffusivity is expressed by the Stejskal-Tanner equation:

$$S(b) = S_0 \cdot e^{-b \cdot D},$$

where:

- $S(b)$  : diffusion-weighted signal,
- $S_0$  : non-diffusion-weighted signal ( $b = 0$ ),
- $b$  : diffusion weighting factor,
- $D$  : apparent diffusion coefficient (ADC).

Reorganizing this equation provides the Apparent Diffusion Coefficient (ADC), which quantifies the overall diffusion rate of water molecules in tissues:

$$ADC_{DWI} = \frac{1}{b} \ln \left( \frac{S(b)}{S_0} \right).$$

### HARDI Data

High Angular Resolution Diffusion Imaging (HARDI) is an advanced diffusion acquisition technique that achieves higher angular resolution by sampling the diffusion signal across a greater number of gradient directions. While traditional diffusion-weighted imaging (DWI) reaches diminishing returns beyond 30 sampled directions, higher-order models such as diffusion tensor imaging (DTI) or constrained spherical deconvolution (CSD) can leverage the additional angular information to more accurately resolve multiple fiber populations within a single voxel. This enhanced angular discernment is crucial for studying complex fiber configurations, such as crossing or branching fibers. [26]

### Multi-Shell DWI

Multi-Shell Diffusion Weighted Imaging (DWI) involves sampling diffusion signals at multiple b-values, capturing diffusion processes across different spatial scales. This approach enhances the ability to distinguish between tissue microstructures by probing varying diffusivity. Multi-shell imaging is not mutually exclusive with HARDI acquisitions; in fact, many studies, including the Human Connectome Project (HCP), employ multi-shell HARDI data to combine the benefits of high angular resolution and multi-scale diffusivity characterization. [26]

### 3.1.2 Diffusion Tensor Model

Although the DWI does provide insight into diffusivity of the tissues, it fails to model anisotropic diffusion which is abundant in the brain. The diffusion tensor characterizes the magnitude and orientation of diffusion in three-dimensional space, offering a more accurate representation of the tissue's microstructure.

For Diffusion Tensor Imaging (DTI), at least six diffusion directions must be sampled to estimate the tensor, but in practice, typical protocols sample more than 30 directions to enhance the accuracy and resolution of the measurements. While this increased sampling enhances data quality, it also necessitates more complex imaging sequences and longer acquisition times.

In contrast to DWI, which primarily quantifies mean diffusivity, DTI yields more detailed information about brain connectivity by analyzing the principal diffusion direction within each voxel. This capability enables advanced techniques, such as tractography, which generates three-dimensional maps of white matter tracts, revealing critical insights into the brain's structural connectivity. [26]

The diffusion tensor is represented as:

$$\mathbf{D} = \begin{bmatrix} D_{xx} & D_{xy} & D_{xz} \\ D_{xy} & D_{yy} & D_{yz} \\ D_{xz} & D_{yz} & D_{zz} \end{bmatrix}$$

Resulting in the Stejskal-Tanner equation for DTI:

$$S(b, \vec{g}) = S_0 \cdot e^{-b \cdot \vec{g}^T \cdot \mathbf{D} \cdot \vec{g}}, \quad (3.1)$$

where:

$S(b, \vec{g})$  : diffusion-weighted signal,  
 $\vec{g}$  : gradient direction vector,  
 $\mathbf{D}$  : diffusion tensor.

### Diffusion Tensor Metrics

The apparent diffusion coefficient (ADC) quantifies the overall diffusion rate of water molecules within tissues. It provides a measure of the restriction or freedom of diffusion, which can be influenced by tissue structure, cellularity, and barriers such as membranes. ADC is calculated similarly for both DTI and DWI, but in DTI, it is specifically derived from the attenuation of the diffusion signal along a single direction. The equation for ADC in DTI is:

$$\text{ADC}_{\text{DTI}} = \frac{1}{b} \ln \left( \frac{S(b)}{S(0)} \right) \quad (3.2)$$

Axial diffusivity (AD) and radial diffusivity (RD) are two key metrics derived from the eigenvalues of the diffusion tensor. Axial diffusivity (AD) reflects the diffusion along the primary direction of water diffusion, which corresponds to the principal eigenvector of the tensor. Radial diffusivity (RD), on the other hand, measures the diffusion perpendicular to the principal eigenvector. These metrics are defined as:

$$\begin{aligned} AD_{DTI} &= \lambda_1 \\ RD_{DTI} &= \frac{\lambda_2 + \lambda_3}{2} \end{aligned} \quad (3.3)$$

where  $\lambda_1, \lambda_2, \lambda_3$  are the eigenvalues of the diffusion tensor, with  $\lambda_1$  being the largest eigenvalue (representing the principal direction of diffusion) and  $\lambda_2, \lambda_3$  representing the perpendicular directions.

Mean diffusivity (MD) is another important metric that reflects the overall diffusion within a tissue, averaging all three eigenvalues of the diffusion tensor. It provides insight into the general mobility of water molecules in a tissue and can indicate pathological changes, such as those seen in neurodegenerative diseases. MD is given by:

$$MD_{DTI} = \frac{\lambda_1 + \lambda_2 + \lambda_3}{3} \quad (3.4)$$

### 3.1.3 Constrained Spherical Deconvolution

Constrained Spherical Deconvolution (CSD) improves on DTI by estimating the fiber orientation distribution function (fODF). This allows CSD to identify multiple fiber orientations within a voxel, making it especially useful for areas where fibers cross or have complex patterns.

CSD works by modeling the measured diffusion signal as the result of a local tissue response function (RF) convolved with the fODF. The RF represents how the signal behaves when there is a single, coherently aligned fiber in a voxel. By deconvolving the measured signal with the RF, the fODF can be recovered, revealing the orientations and relative amounts of different fibers.

$$S(\theta, \phi) = \sum_i f_i \cdot A_i \cdot R(\theta) \quad (3.5)$$

where:

- $S(\theta, \phi)$  is the measured signal in direction  $(\theta, \phi)$ ,
- $f_i$  is the volume fraction of fiber population  $i$ ,
- $A_i$  is the rotation matrix for direction  $(\theta, \phi)$ ,
- $R(\theta)$  is the response function with elevation  $\theta$  and fixed  $\phi$ .

The key advantage of CSD over DTI is its ability to resolve multiple fiber orientations in each voxel, even when fibers cross or spread in different directions, without needing an estimate of the number of fibers; instead, it uses deconvolution to directly recover the fODF from the data. The tissue response function, based on empirical data, describes signal attenuation for a single fiber, accounting for both axial and radial diffusivity, though CSD assumes constant anisotropy across the brain, which may overlook some tissue variations but is effective for many applications. A critical feature of CSD is the non-negativity constraint applied during deconvolution, ensuring that the fODF remains positive since negative fiber orientations are not physically possible. CSD is particularly useful for investigating regions with complex fiber arrangements and provides more accurate results in areas where DTI may fail to capture multiple fibers in a voxel. [28]

### MSMT-CSD

Multi-Shell Multi-Tissue CSD (MSMT-CSD) [29] goes a step further and makes use of multi shell data, exploiting the b-value dependency of tissue response to estimate the fraction and contribution of multiple tissue types. Typically the modelled tissues are white matter, gray matter and CSF. Gray matter and CSF are modeled as isotropic, while white matter remains anisotropic. In the case of MSMT-CSD, the signal model becomes:

$$S(\theta, \phi, b) = \sum_t \sum_i f_{t,i} \cdot A_{t,i}(b) \cdot R_t(\theta) \quad (3.6)$$

where:

- $S(\theta, \phi, b)$  is the measured signal in direction  $(\theta, \phi)$  and b-value  $b$ ,
- $f_{t,i}$  is the volume fraction of tissue type  $t$  in fiber population  $i$ ,
- $A_{t,i}(b)$  is the tissue-specific response function for b-value  $b$  and tissue type  $t$ ,
- $R_t(\theta)$  is the tissue-specific response function.

## 3.2 Diffusivity Metrics

Now that the orientation of the PVS is available it can be applied to the estimation of diffusivity in the PVS. However, there is a resolution mismatch; the vector field has a resolution of 0.7 mm, and the diffusion data is at 1.2 mm. Generally the structural image would now be downsampled via interpolation to match the diffusion resolution. However, given the scarcity of the PVS segmentation, downsampling would result in significant loss of information. To mitigate this, the diffusion image was upscaled to match the vector field's resolution, though this results in a large image, often exceeding 10GB. While the image size could be reduced by creating an upscaled PVS mask within the diffusion data, the whole-brain image was retained for simplicity and visualization purposes.

Initially, MSMT-CSD is employed to explore the composition of PVS-containing voxels. Following this, three models for estimating PVS diffusivity are presented: a simple model using a standard DTI image, a multi-tensor model that fits separate tensors for both white matter and PVS orientations, and a constrained multi-tensor model in which the PVS tensor is fixed to the determined vector orientation.

### 3.2.1 Qualitative Analysis of PVS Environment Using MSMT CSD

The MSMT CSD method from the Mrtrix3 package [30] was applied to the voxels containing the PVS to examine the relationship between the PVS and white matter, specifically investigating whether the PVS tends to align with white matter fibers and the number of fiber tracts typically present in a segmented voxel. This analysis helps assess the validity of assumptions made for the PVS metrics.

This analysis is purely qualitative due to the violation of several key assumptions inherent in the MSMT CSD model. Since there is no dedicated response function for the PVS, it is modeled as white matter, which introduces bias into the estimation of component fractions. Additionally, the fODF may not capture the PVS signal effectively. If the PVS signal is small, it may be filtered out by the non-negativity constraint. On the other hand, if the signal is large, it may interfere with the estimation of white matter. In cases where the PVS is identified as a separate peak, its estimation is likely to be poor due to its larger radial diffusivity compared to the response function. Despite these challenges, the model may still yield reasonable estimates for fiber count and orientation.

Figure 3.2 shows an in-vivo fODF in a segmented voxel with multiple white matter orientations.

To further evaluate the fODF, Mrtrix3's sh2peaks tool was used to determine the magnitude of the five largest peaks and the closest peak to the PVS vector, as shown in Figure 3.3. The closest peak to the PVS vector was compared to the actual PVS orientation by calculating the absolute value of their cosine similarity. The absolute value was used to account for the bidirectional nature of orientation vectors. The analysis revealed a mean correlation of 0.9067 with a standard deviation of 0.092. Approximately 40% of the PVS voxels had a similarity score greater than 0.95. While this seems significant, it should be noted that CSD frequently produces numerous small bidirectional peaks, resulting in a crowded angular space.

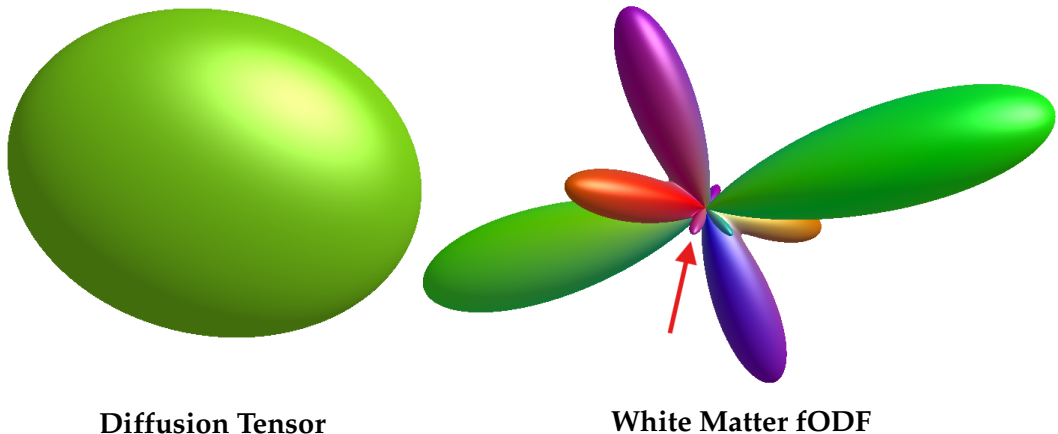
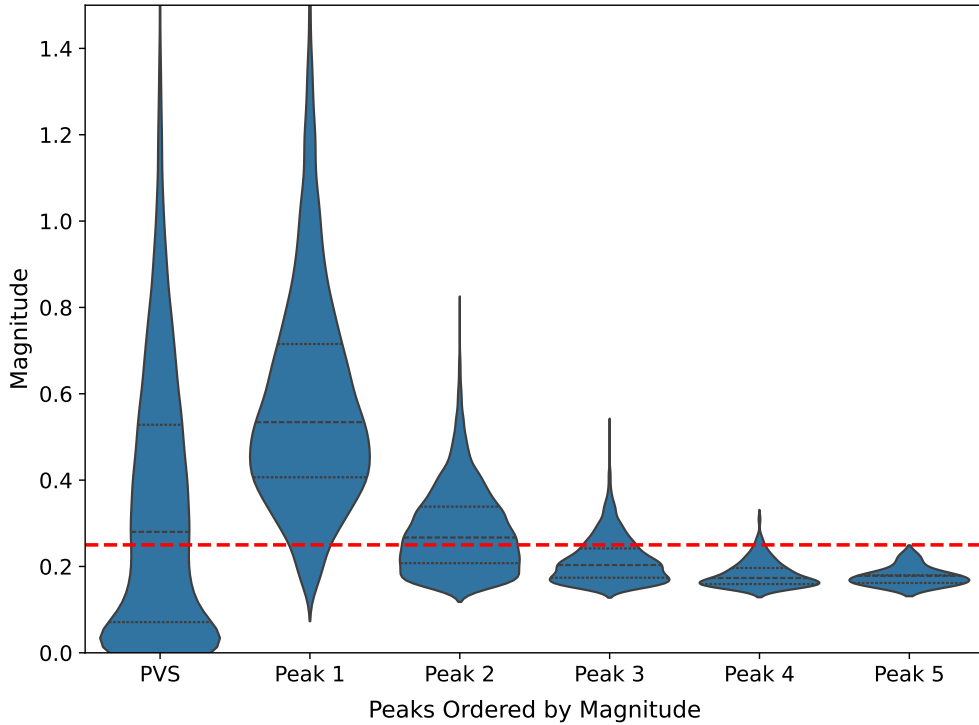


FIGURE 3.2: DTI vs fODF. This visualization is from a single PVS containing voxel containing multiple white matter tracts. On the left is the estimated diffusion tensor. On the right is the fODF for the white matter estimated using CSD. The arrow points to the peak which closely matches PVS orientation.



**FIGURE 3.3: PVS and White Matter fODF peaks.** This is a probability density estimation of the 5 most significant peaks in the fODF of PVS containing voxels. The PVS peak is the closest peak to the orientation of the PVS. The red line demonstrates an approximate threshold where peaks are likely to be white matter.

### 3.2.2 Apparent Diffusion along PVS Orientation

The first metric attempted and the simplest by far is simply evaluating the tensor in each voxel along the orientation of the PVS. This is somewhat similar to DTI-ALPS in that it is measuring the diffusivity of all tissues along that orientation. However, unlike DTI-ALPS there is no assumption of white matter direction. Despite this limitation, the metric may still be useful for quantifying broad changes in diffusivity, provided there is a sufficiently thorough and accurate segmentation of the PVS. In order to improve on this the signal contribution of the PVS will need to be separated from the other tissues.

### 3.2.3 Multi-Tensor Modelling

The Stejskal-Tanner equation (3.1) can be extended to model the signal as the sum of contribution from multiple tensors weighted by their volume fraction. This allows separate diffusivity estimates for multiple components. Here component refers to any unique tissue and/or orientation such that it has a distinct diffusion response within the voxel. By modeling the voxel as the sum of signal contributions, we have:

$$S(b, \vec{g}) = S_0 \sum_{i=1}^n f_i \left( e^{-b \cdot \vec{g}^T \mathbf{D}_i \vec{g}} \right) \quad \sum_{i=1}^n f_i = 1, \quad (3.7)$$

where:

- $f_i$  : volume fraction of the  $i$ -th component,
- $\mathbf{D}_i$  : diffusion tensor of the  $i$ -th component (6 DOF).

The volume fraction  $f_i$  reflects the effective contribution of a tensor to the measured signal and is not purely determined by the component's anatomical volume. For example, the PVS occupies a small proportion of its segmented volume. However, due to signal attenuation within the vasculature, it does not contribute significantly to the diffusion signal. This discrepancy arises because signal attenuation depends on the intrinsic diffusion properties of each component and the strength of the applied diffusion gradients.

In this context, components with restricted or hindered diffusion, like white matter (WM), may dominate the signal despite occupying a similar or smaller anatomical volume than other components. Consequently, effective volume fractions in multi-tensor models are determined not only by the anatomical volume but also by diffusion weighting and the microstructural characteristics of each components.

For determining diffusion in the PVS a two tensor model will be used, estimating one white matter component and the PVS.

$$S(b, \vec{g}) = S_0 \left[ f_{\text{PVS}} (e^{-b \cdot \vec{g}^T \mathbf{D}_{\text{PVS}} \vec{g}}) + (1 - f_{\text{PVS}}) (e^{-b \cdot \vec{g}^T \mathbf{D}_{\text{WM}} \vec{g}}) \right] \quad (3.8)$$

where:

- $f_{\text{PVS}}$  : volume fraction of the PVS,
- $\mathbf{D}_{\text{PVS}}$  : diffusion tensor of the PVS (6 DOF),
- $\mathbf{D}_{\text{WM}}$  : diffusion tensor of the WM (6 DOF),

### 3.2.4 Multi-Tensor Modelling with Constrained PVS Angle

The above models use the vector-field of PVS orientations to sample the tensors estimated from the diffusion data. However, given that we have prior knowledge of the PVS orientation it should be possible to estimate a more accurate tensor for the PVS. This constraint also reduces the risk that the PVS tensor will be fit to the white matter and vice versa.

By constraining the PVS tensor along the vector field orientation we can simplify the model to two degrees of freedom, axial and radial diffusivity. Assuming  $\lambda_2 = \lambda_3$  is reasonable for PVS due to its tubular structure.

By fixing the PVS tensor along the known vector-field orientation, we can simplify the model to just two degrees of freedom: axial and radial diffusivity. This simplification is justified by the tubular structure of the PVS, which typically exhibits highly anisotropic diffusion along its axis and isotropic or near-isotropic diffusion in the radial direction. As such, assuming that the radial diffusivities,  $\lambda_2$  and  $\lambda_3$ , are equal is reasonable for the PVS, providing a more efficient and constrained estimation.

Incorporating these constraints into equation 3.8 results in:

$$S(b, \vec{g}) = S_0 \left[ f_{\text{PVS}} \cdot e^{-b \cdot \vec{g}^T \cdot (\mathbf{R} \cdot \mathbf{D}_{\text{PVS}} \cdot \mathbf{R}^T) \cdot \vec{g}} + (1 - f_{\text{PVS}}) \cdot e^{-b \cdot \vec{g}^T \cdot \mathbf{D}_{\text{WM}} \cdot \vec{g}} \right] \quad (3.9)$$

where:

$\mathbf{R}$  : rotation matrix describing the orientation of the PVS tensor,  
 $\mathbf{D}_{\text{PVS}} = \text{diag}(D_{\text{axial}}, D_{\text{radial}}, D_{\text{radial}})$

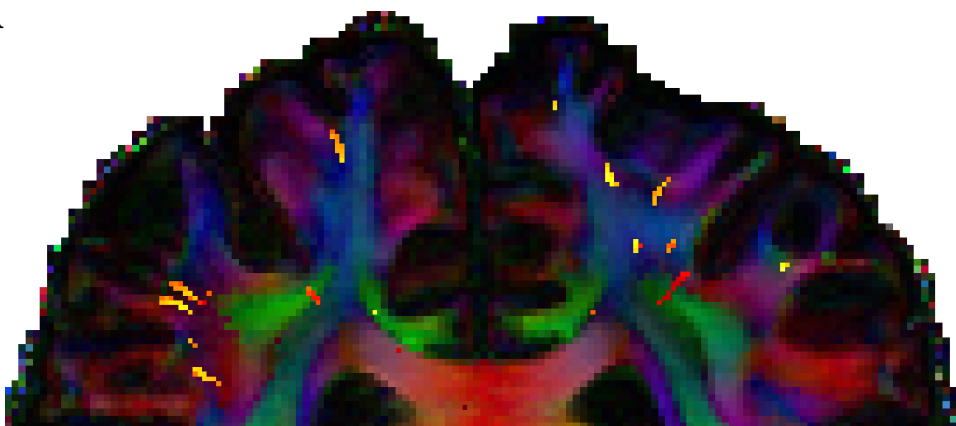
### 3.2.5 In-vivo: Single-Tensor vs Constrained-Multi-Tensor Model

The Single-Tensor and Constrained-Multi-Tensor models were applied to in-vivo upscaled HCP diffusion data. The exact implementation of these models is discussed in more detail in Section 1.3 below. Table 3.1 below also includes the results of normalizing the Constrained-Multi Tensor estimate by the volume fraction of PVS.

Method	Mean	Std Dev	Min	Max
Single-Tensor	0.7657	0.2663	0.033	2.681
Constrained Multi-Tensor	1.1340	0.1420	1.001	1.299 $\times 10^{-3}$ mm <sup>2</sup> /s
CMT Normalised	2.7345	0.2473	1.001	3.022
CMT Volume Fraction	0.4134	0.0142	0.400	0.4299

TABLE 3.1: Summary statistics for in-vivo application of PVS Models.

A



B

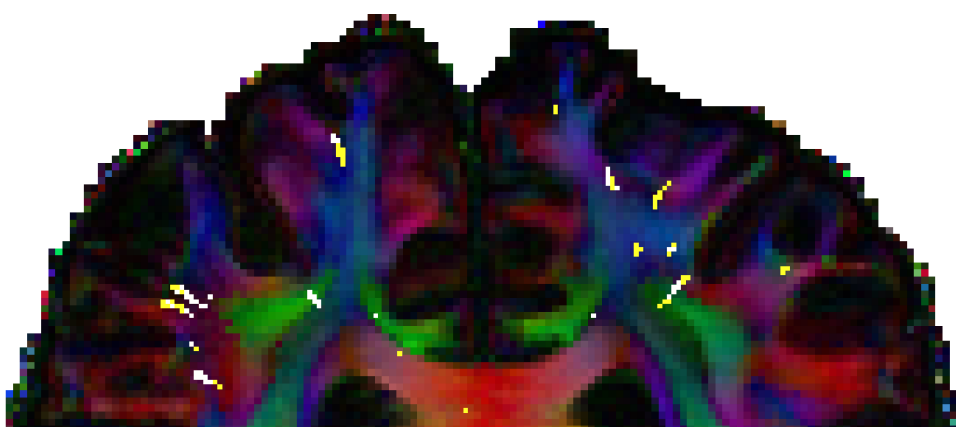


FIGURE 3.4: Comparison of Single-Tensor and Multi-Tensor Diffusion Models. Both models are overlayed on an eigenvector contrast used to visualize white matter orientation. Image A is the ADC along PVS for the single tensor model. Image B is the ADC along PVS estimated from PVS diffusion tensors estimated using the constrained multi-tensor model.

### 3.3 Simulation

Although in-vivo results provide interesting insights into the macro-behavior of diffusion models, uncovering the underlying causes of specific behaviors can be challenging. To achieve a more quantitative comparison of models, a simpler single voxel model is required. This model will enable better control over parameters and provide clearer insights into the causes behind observed behaviors.

For these simulations, only a single white matter fiber tract will be modeled in the PVS voxel. While extending to additional white matter fiber orientations is possible—requiring only an extra tensor under the same assumptions and response function—this increases the complexity of the problem and the behavior. Resolving additional tensors can be achieved through various techniques, such as targeted use of multi-shell data or localized response functions. However, these approaches are outside the scope of this simulation, as they are equally applicable to all multi-tensor models.

To begin the simulation, two ground truth tensors are created: one for white matter (WM) and one for the PVS. The diffusivity values are chosen to approximate real-world values. The volume fraction of PVS is arbitrary, as the diameter of PVS can vary widely; this simulation will consider a range from negligible PVS to total PVS, with all values being reasonable within the biological context. For white matter, an axial diffusivity of  $2.0 \times 10^{-3} \text{ mm}^2/\text{s}$  and a radial diffusivity of  $0.5 \times 10^{-3} \text{ mm}^2/\text{s}$  will be used.

The ground truth model for PVS is informed by its physiological structure and composition. The PVS is a tubular structure filled with CSF-like fluid, which leads to distinct diffusion characteristics when compared to white matter. The fluid-filled, tubular morphology of the PVS suggests that its axial diffusivity should be slightly higher than that of white matter. This is because the unhindered flow of water molecules along the primary axis of the tube is less restricted compared to the densely packed, myelinated fibers in white matter. A reasonable estimate for the axial diffusivity of PVS is approximately  $2.5 \times 10^{-3} \text{ mm}^2/\text{s}$ .

Furthermore, the PVS's tubular geometry supports a relatively higher radial diffusivity compared to the tightly bundled, anisotropic white matter. In white matter, radial diffusivity is constrained by myelin and tightly packed axonal fibers, while in the PVS, the diffusion of water molecules perpendicular to the tube's axis faces fewer barriers. Based on these considerations, a radial diffusivity value of approximately  $1.0 \times 10^{-3} \text{ mm}^2/\text{s}$  is a reasonable estimate for PVS.

Several key questions drive these simulations:

- What is the response of the single-tensor model to change in WM angle?
- What is the effect of noise on the estimation of PVS characteristics?
- How much do multi-tensor models improve the estimation?
- How does prior knowledge of PVS orientation impact the accuracy?
- How significant is the accurate estimation of fractional anisotropy?

### 3.3.1 Estimating Signal from Tensors

The signal attenuation for each gradient direction and b-value is computed using the Stejkal-Tanner equation (3.1) for a two-tensor model consisting of white matter (WM) and perivascular space (PVS). The attenuation is calculated by applying the diffusion tensor for both tensors to the gradient direction vector. Assuming unit proton density you the signal attenuation can be modelled as:

The forward model computes the signal attenuation for each gradient direction and b-value using a two-tensor model consisting of white matter (WM) and perivascular space (PVS). The total signal is computed by applying the diffusion tensor for each tensor to the gradient direction vector.

Assuming unit proton density, the signal attenuation is modeled as follows:

$$S(b, \vec{g}) = f_{\text{WM}} \cdot S_{\text{WM}}(b, \vec{g}) + f_{\text{PVS}} \cdot S_{\text{PVS}}(b, \vec{g}) + \epsilon, \quad (3.10)$$

where  $\epsilon$  represents the noise added to the signal. The noise component  $\epsilon$  is modeled as Gaussian noise, which is added to the total signal when the SNR is finite.  $\epsilon$  is generated as Gaussian noise with zero mean and variance  $\frac{S(b, \vec{g})}{\text{SNR}}$ .

$$\epsilon = \mathcal{N} \left( 0, \frac{S(b, \vec{g})}{\text{SNR}} \right), \quad (3.11)$$

For the perivascular space (PVS) compartment, the diffusion tensor is the diagonal diffusion tensor of the PVS compartment:

$$\mathbf{D}_{\text{PVS}} = \text{diag}(\lambda_{\parallel}, \lambda_{\perp}, \lambda_{\perp}),$$

The signal attenuation for the PVS compartment is then modeled as:

$$S_{\text{PVS}}(b, \vec{g}) = e^{-b \cdot \vec{g}^T \cdot \mathbf{D}_{\text{PVS}} \cdot \vec{g}}, \quad (3.12)$$

For the white matter (WM) compartment, the diffusion tensor is given by:

$$\mathbf{D}_{\text{WM}} = \text{diag}(2.0 \times 10^{-3}, 0.5 \times 10^{-3}, 0.5 \times 10^{-3}),$$

The signal attenuation for the WM compartment is modeled as:

$$S_{\text{WM}}(b, \vec{g}) = e^{-b \cdot \vec{g}^T \cdot (\mathbf{R} \cdot \mathbf{D}_{\text{WM}} \cdot \mathbf{R}^T) \cdot \vec{g}}, \quad (3.13)$$

The rotation matrix  $\mathbf{R}$  is defined as:

$$\mathbf{R}_z(\alpha) = \begin{bmatrix} \cos(\alpha) & -\sin(\alpha) & 0 \\ \sin(\alpha) & \cos(\alpha) & 0 \\ 0 & 0 & 1 \end{bmatrix} \quad (3.14)$$

### 3.3.2 Recovering Tensor from Estimated Signal

The signal attenuation, estimated from the ground truth tensors, represents the actual signal observed during acquisition, excluding the influence of other tissues and imaging artifacts. By fitting diffusion tensors to this measured signal, we can directly assess the discrepancy between the ground truth and the estimated tensors.

This fitting process involves solving the Stejkal-Tanner equation (3.1) in reverse, using the least-squares method to estimate the diffusion tensor parameters based on the observed data. The least-squares cost function for this fitting process is defined as the sum of squared errors between the measured and predicted signals, where the signal attenuation at each gradient direction and b-value is modeled using the diffusion model. The cost function is expressed as:

$$\text{Cost} = \sum_{\vec{g}} \sum_b \left( S_{\text{measured}} - S_{\text{predicted}} \right)^2 \quad (3.15)$$

This cost function quantifies the difference between the observed signals and those predicted by the diffusion model, and its minimization leads to an optimal set of diffusion tensor parameters.

In addition to minimizing the error, the optimization process incorporates constraints to ensure the diffusion tensors remain positive semi-definite. This is achieved by checking the eigenvalues of each diffusion tensor and applying a penalty if any eigenvalue is negative.

The system of equations used to estimate the parameters is given by:

$$\mathbf{A} \cdot \mathbf{p} = \mathbf{b} \quad (3.16)$$

where:

- $\mathbf{A}$  is the matrix of coefficients derived from the diffusion gradients and b-values.
- $\mathbf{p}$  is the vector of unknown parameters, which includes the tensor values to be estimated.
- $\mathbf{b}$  is the vector of logarithms of the measured signals, adjusted for the b-values.

The optimal parameters  $\mathbf{p}$  are obtained by solving this system using the least-squares method:

$$\mathbf{p} = (\mathbf{A}^T \mathbf{A})^{-1} \mathbf{A}^T \mathbf{b} \quad (3.17)$$

### 3.3.3 Experiments

The simulations used the same sampling scheme as the HCP HARDI data, with 90 directions across three shells. The measured error value is the percent difference between the axial diffusivity of the PVS and the measured axial diffusivity from the modelled tensor. The parameters to fit for each model are shown in table 3.2. Three distinct experiments were conducted with their conditions presented in table 3.3.

**Varying a Single Parameter:** This experiment measures the error as a single variable changes. It was evaluated at three different SNRs: infinite SNR, 50, and 20. The finite values represent typical ranges from MRI diffusion imaging.

**Axial and Diffusivity:** In this simulation, the axial and radial diffusivity are simultaneously varied to simulate PVS with fractional anisotropy ranging from 0 to 1, and diffusivity ranging from free to highly restricted. While these extremes are physiologically unrealistic for PVS, they serve to demonstrate model behavior when incorrect structures are segmented.

**Varying Fractional Volume and White Matter Angle:** This experiment focuses on the impact of varying fractional volume and the white matter angle. These two variables do not maintain consistency in vivo, unlike diffusivity. The error resulting from these variations will provide insights into the performance of the model under ideal conditions with a known PFS anisotropy.

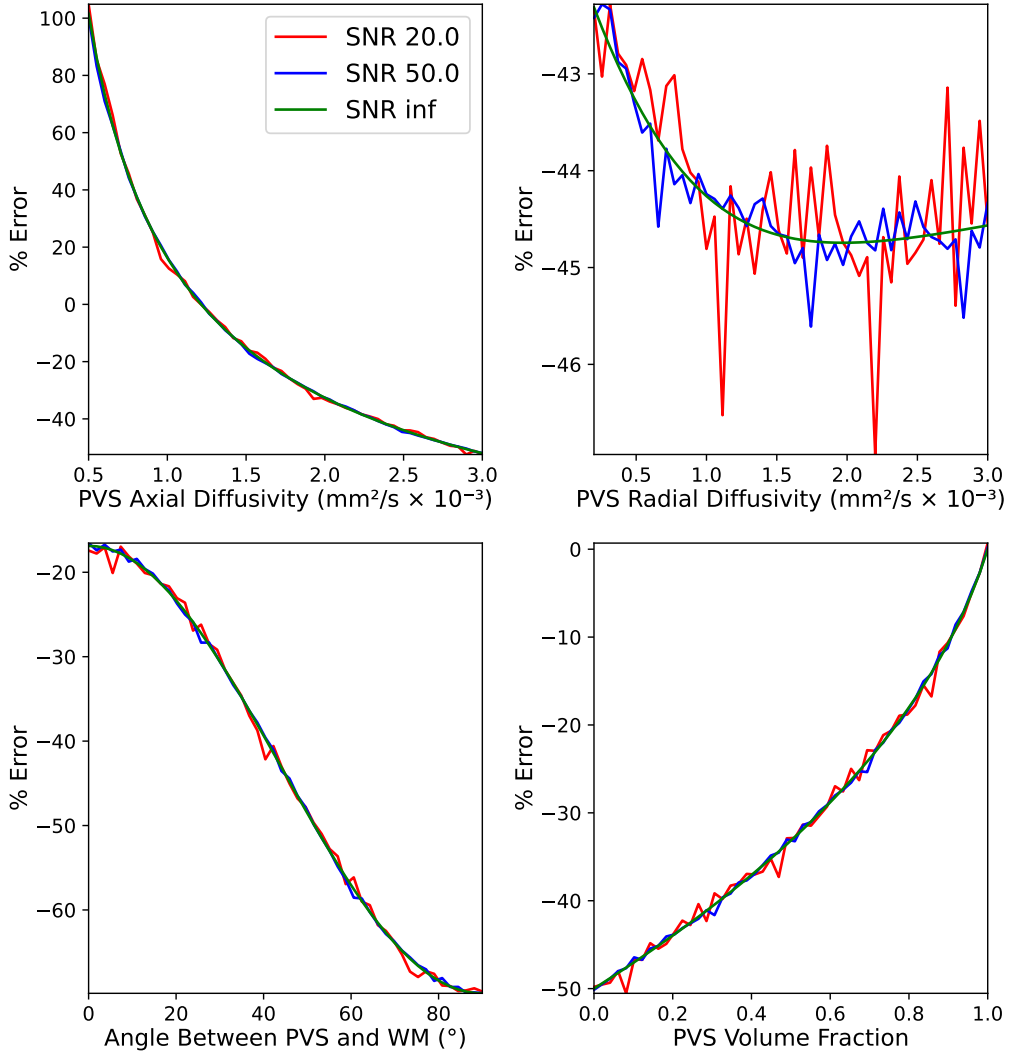
Model Type	Parameters	Total DOF
<b>Single-Tensor</b>	$\mathbf{D}_{WM}$ (6 DOF)	6
<b>Multi-Tensor</b>	$f_{PVS}, \mathbf{D}_{WM}$ (6 DOF), $\mathbf{D}_{PVS}$ (6 DOF)	13
<b>Constrained Multi-Tensor</b>	$f_{PVS}, \mathbf{D}_{WM}$ (6 DOF), $\mathbf{D}_{PVS}$ (2 DOF)	9

TABLE 3.2: List of parameters and degrees of freedom (DOF) for the Single-Tensor, Multi-Tensor, and Constrained Multi-Tensor Models. Total DOF is the sum of all independent parameters.

Parameter	SNR	Diffusivity	Volume-Alpha
PVS $\lambda \parallel$ ( $\text{mm}^2/\text{s}$ )	$5 \times 10^{-4}$ to $3 \times 10^{-3}$	$5 \times 10^{-4}$ to $3 \times 10^{-3}$	$2.5 \times 10^{-3}$
PVS $\lambda \perp$ ( $\text{mm}^2/\text{s}$ )	$2 \times 10^{-4}$ to $3 \times 10^{-3}$	$2 \times 10^{-4}$ to $1.5 \times 10^{-3}$	$1 \times 10^{-3}$
WM $\lambda \parallel$ ( $\text{mm}^2/\text{s}$ )	$2 \times 10^{-3}$	$2 \times 10^{-3}$	$2 \times 10^{-3}$
WM $\lambda \perp$ ( $\text{mm}^2/\text{s}$ )	$5 \times 10^{-4}$	$5 \times 10^{-4}$	$5 \times 10^{-4}$
$f_{PVS}$ (0 to 1)	0 to 1	0.2	0 to 1
$\alpha$ (degrees)	$0^\circ$ to $90^\circ$	$45^\circ$	$0^\circ$ to $90^\circ$

TABLE 3.3: Parameter Ranges and Defaults for Experiments

### 3.3.4 SNR Comparison



**FIGURE 3.5: Simulation of Single Compartment Tensor Reconstruction.** Error in estimating axial diffusivity using the recovered tensor is compared against the ground truth axial diffusivity. There appears to be no non-linear effects from decreased SNR.

### 3.3.5 Diffusivity and Volume-Alpha Comparison

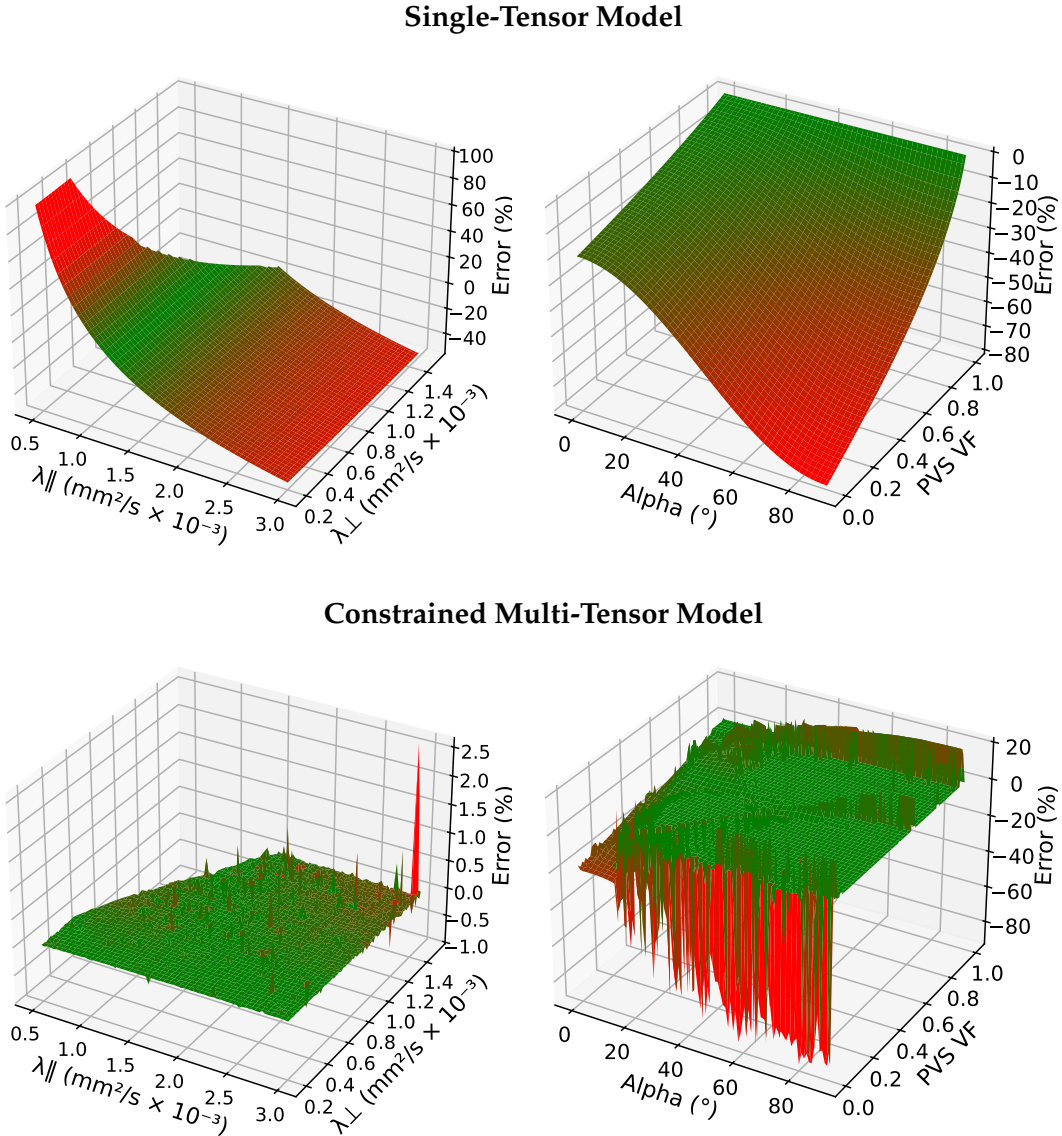


**FIGURE 3.6: Comparison of Single-Tensor and Multi-Tensor Diffusion Models.** Error in estimating axial diffusivity using the recovered tensor is compared against the ground truth axial diffusivity. Colormap is normalized to be green at 0% error.

# **Chapter 4**

## **Discussion**

This study aimed to combine a structural segmentation-derived vector field with diffusion-weighted imaging (DWI) to estimate quantitative diffusion metrics in the PVS globally, in contrast to the current ROI based qualitative metrics like DTI-ALPS. This chapter will discuss the results of the analysis performed, their significance and limitations, followed by the next steps in evaluating PVS diffusion.

### **4.1 Segmentation**

The automated segmentation model, WPSS, outperformed the heuristic model as anticipated. WPSS successfully captured finer juxta-cortical PVS and additional PVS in the centrum semiovale. One of the key advantages of WPSS was that it did not require a mask, unlike the Frangi filter. Occasionally, sufficiently large PVS would be excluded from the white matter mask by the parcellation tool; however, with WPSS, no mask was required, allowing for appropriate segmentation of these regions.

Based on visual scoring, the following recommendations could be implemented to improve WPSS:

- Masking the Pons and Medulla Oblongata to avoid segmenting these regions, as they are extremely noisy on the EPC and typically contain no visible PVS.
- Expanding the maximum sigma range to capture the extremely enlarged spaces.
- Normalizing or rejecting extreme outliers in white matter contrast.

Otherwise, the accuracy of the segmentation was exceptional, with little need for quality control. Given the excellent results of WPSS, any substantial improvements in PVS segmentation are more likely to come from better acquisition methods or the use of more specialized contrasts.

## 4.2 Evaluating the Constrained-Multi-Tensor Model

The Constrained Multi-Tensor (CMT) model performed surprisingly well on in vivo data. It was anticipated that modeling a single white matter tensor would result in significant performance variability across regions dominated by a single fiber versus regions with complex fiber configurations. However, as illustrated in Figure 3.4, the CMT model demonstrated remarkable stability, even in areas with crossing white matter tracts. This suggests that the simplified single-tensor approximation adequately captures the signal in most cases.

Figure 3.3 highlights the sharp decline in the magnitude of the second and third white matter peaks, with the estimated fODF indicating that most PVS voxels contain a single dominant white matter fiber and occasional smaller crossing fibers. The presence of a second distinct fiber may bias the optimization, but such effects appear negligible in practice.

Interestingly, the model estimated PVS axial diffusivity at  $1.13 \times 10^{-3} \text{ mm}^2/\text{s}$ , which is considerably lower than expected. When normalized by the volume fraction, the mean axial diffusivity rose to  $2.73 \times 10^{-3} \text{ mm}^2/\text{s}$ , a more reasonable but slightly elevated value. This discrepancy suggests that the volume fraction of the PVS is being significantly underestimated. Assuming the true axial diffusivity is closer to  $2.5 \times 10^{-3} \text{ mm}^2/\text{s}$ , as indicated by simulations, the appropriate PVS volume fraction in these voxels would be approximately 90%, rather than the estimated 41%.

Simulations also demonstrated that the axial and radial diffusivities of the PVS have minimal impact on the model's ability to estimate axial diffusivity. This finding is particularly significant given the large variability in PVS diffusivity, which can increase tenfold during sleep. However, the simulations uncovered a notable limitation of the multi-tensor model: when the white matter angle is within approximately  $15^\circ$  of the PVS orientation, the PVS diffusivity is underestimated by up to 20% (see Figure 3.6). Additionally, an unexplained overestimation of diffusivity occurs when white matter and PVS have equal volume fractions.

The initial simulations, while useful, were overly simplistic. Future simulations should incorporate additional components, including an isotropic compartment to represent CSF and gray matter, as well as one to two additional white matter components.

The constrained multi-tensor model offers a foundation but leaves room for refinement. Introducing radial symmetry to white matter, constraining anisotropy, could further simplify the fitting process, albeit with some loss of accuracy. Extending the model to account for  $n$ -components of white matter is another possibility, though it presents significant challenges, as discussed in Section 4.3.3.

## 4.3 Next Steps

### 4.3.1 Multi-Modal Segmentation

The use of EPC contrast significantly improved the visualization of PVS compared to T2-weighted imaging alone. This enhanced contrast facilitates more accurate detection and delineation of PVS, creating new opportunities to study their structure and function. During segmentation validation, susceptibility-weighted imaging (SWI) was compared to EPC to assess complementary information. As shown in Figure 2.2, 7T SWI and EPC may provide complementary insights into PVS visualization. Comparing PVS locations identified with SWI further supports the hypothesis that most visible PVS are periarterial rather than perivenous. In SWI, the majority of PVS were either not visible or exhibited high intensity, a characteristic suggestive of arterial blood. A study by George et al. (2021) [13] highlighted the potential of high-resolution 7T SWI in PVS research. Using an anisotropic resolution of  $0.21 \times 0.21 \times 0.5$  mm, SWI enabled the creation of detailed masks capable of detecting and differentiating periarterial and perivenular spaces. This approach demonstrates SWI's capability not only in visualizing PVS but also in distinguishing between periarterial and perivenular spaces. Moreover, the higher resolution of 7T SWI, which can achieve sub-0.5 mm resolutions, may enable the detection of non-enlarged PVS, facilitating measurements of physiologically normal PVS. This advancement offers an opportunity to investigate the role of smaller, non-pathological PVS that are often undetectable with lower-resolution imaging. Implementing periarterial and perivenous segmentation based on susceptibility will likely require quantitative susceptibility mapping (QSM). Unlike SWI, QSM is solely phase-dependent, leading to reduced inter-subject variability [21]. While SWI is phase-masked to suppress venous signals—hence its colloquial reference as a "venogram"—QSM directly quantifies the degree of paramagnetic and diamagnetic susceptibility. This quantitative capability may enhance segmentation accuracy, allowing for more precise characterization of periarterial and perivenous PVS.

### 4.3.2 Tractography-based Orientation

With a more comprehensive segmentation, the next step would involve leveraging PVS physiology to refine vessel orientation estimation. The PVS can be assumed to have a smoothly varying diameter. However, current segmentation often exhibits bulges, which are likely artifacts caused by partial segmentation near the threshold rather than true structural widening. A spline-based vector map could mitigate these issues by fitting a centerline to each segmented tube and modeling its width based on the average distance from the centerline to adjacent segmented voxels. This approach would support a tractography-like method, enabling the enforcement of anatomical constraints. For instance, PVS pathways should not terminate in the centrum semiovale but should instead extend toward the ventricles.

#### 4.3.3 Combined Diffusion Model

The multi-tensor models typically assume a fixed number of white matter components per voxel. In an ideal scenario, the model would automatically estimate the appropriate number of white matter components for each voxel and calculate their orientations. However, adding each white matter fiber introduces 7 additional degrees of freedom (DOF). This quickly becomes impractical. For example, if the number of gradient directions increases linearly with DOF, a PVS + 5-WM tensor model would require more than 150 directions to achieve the same accuracy as a single tensor model estimated using standard DWI.

For this reason, constrained spherical deconvolution (CSD) has become the more commonly used technique for modeling complex fiber orientations. Unlike multi-tensor models, CSD estimates the number of components without prior assumptions and solves a linear least squares problem, reducing DOF. Each component is represented by a fraction of a response function, rotated by two angles, which significantly reduces computational complexity. However, CSD does require a local tissue model. Estimating these models for white matter, gray matter, and CSF is straightforward, but constructing a general model for the perivascular space (PVS) is more challenging. There is no guarantee that the diffusion response in enlarged PVS regions will represent the entire range of PVS diffusion characteristics. As the PVS enlarges, the volume of free diffusion within these spaces increases, approaching the diffusion characteristics of CSF in very large spaces.

A study by George et al. (2021) [13] investigated a combined diffusion model where CSD was used to estimate the number and initial orientations of white matter components. This information was then used to initialize a multi-tensor model, creating a combined approach that balanced efficiency and accuracy.

This combined approach is particularly well-suited for modeling PVS diffusivity. CSD could be employed to estimate the count and approximate orientation of white matter components, while the PVS orientation derived from the vector field would inform a multi-tensor model. It remains to be determined whether CSD can accurately estimate the white matter angles in PVS-containing voxels. If not, the combined model would still benefit from incorporating an estimate of the white matter component count.

This hybrid multi-tensor-CSD model offers a flexible, efficient solution for PVS modeling. It leverages the speed and versatility of CSD without the need for a local response function for PVS, making it applicable to any brain region.

## 4.4 Conclusion

This study aimed to develop a global diffusion metric for the PVS, derived by combining high-resolution structural imaging with diffusion-weighted imaging (DWI). The segmentation process was successfully implemented and validated using a custom visual scoring methodology. A Hessian-based filter was applied to derive the vector field representing PVS orientations by calculating the direction of minimum curvature. This orientation was then used to constrain a multi-tensor model of PVS diffusion. The model was validated through in-vivo imaging and simulated across a range of physiological conditions. By incorporating both the location and orientation of the PVS, this integrated approach greatly simplifies diffusion modeling. This represents a significant advancement in quantifying diffusion metrics directly from the PVS, providing new insights into the mechanisms underlying paravenous transport in the brain.

## Appendix A

# Supplemental Results

The codebase for this study can be found at:

<https://github.com/CallumCoffey/Disentangling-PVS-Diffusion>

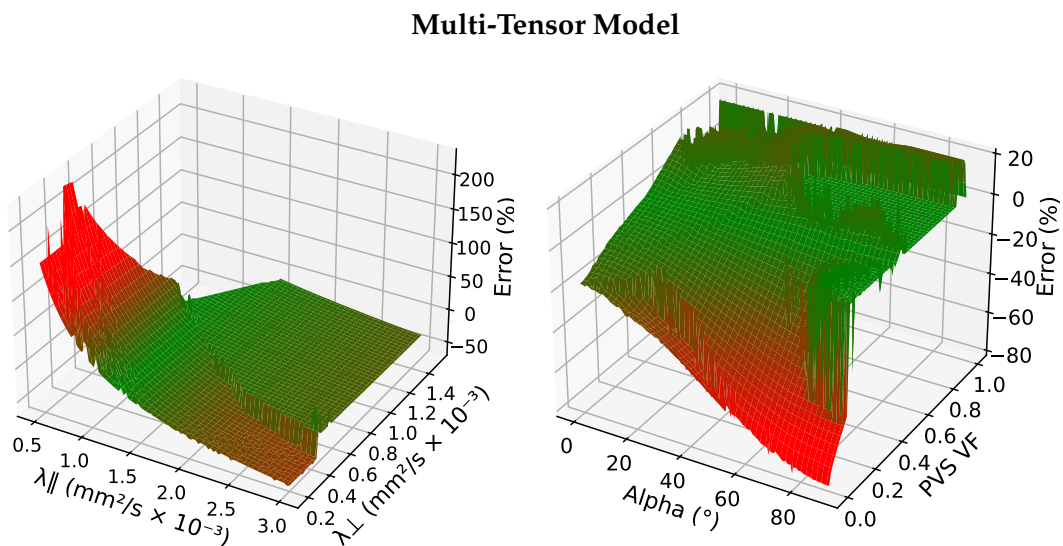


**FIGURE A.1: Results of Multi-Tensor Simulation.** Error in estimating axial diffusivity using the recovered tensor is compared against the ground truth axial diffusivity. Colormap is normalized to be green at 0% error.

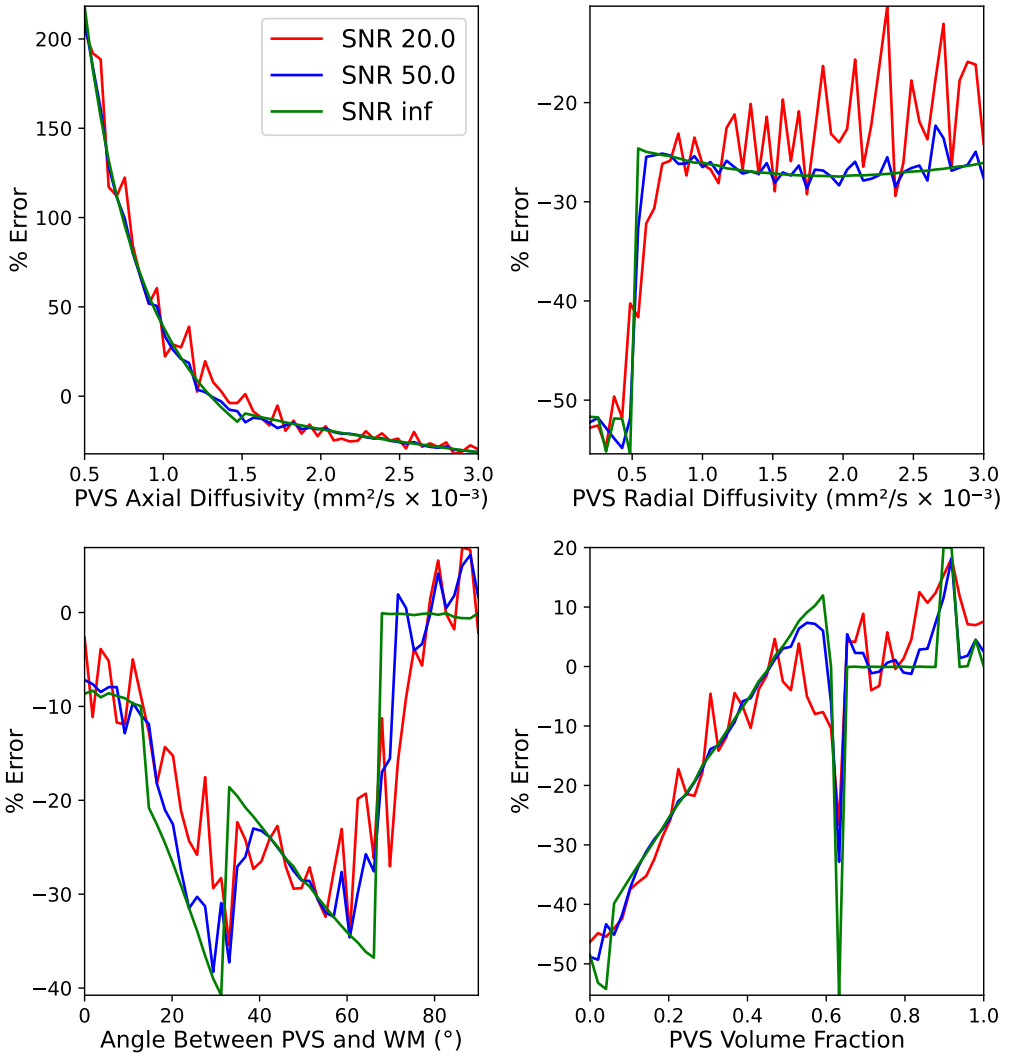


**FIGURE A.2: Simulation of Multi Compartment Tensor Reconstruction.** Error in estimating axial diffusivity using the recovered tensor is compared against the ground truth axial diffusivity. There appears to be no non-linear effects from decreased SNR.

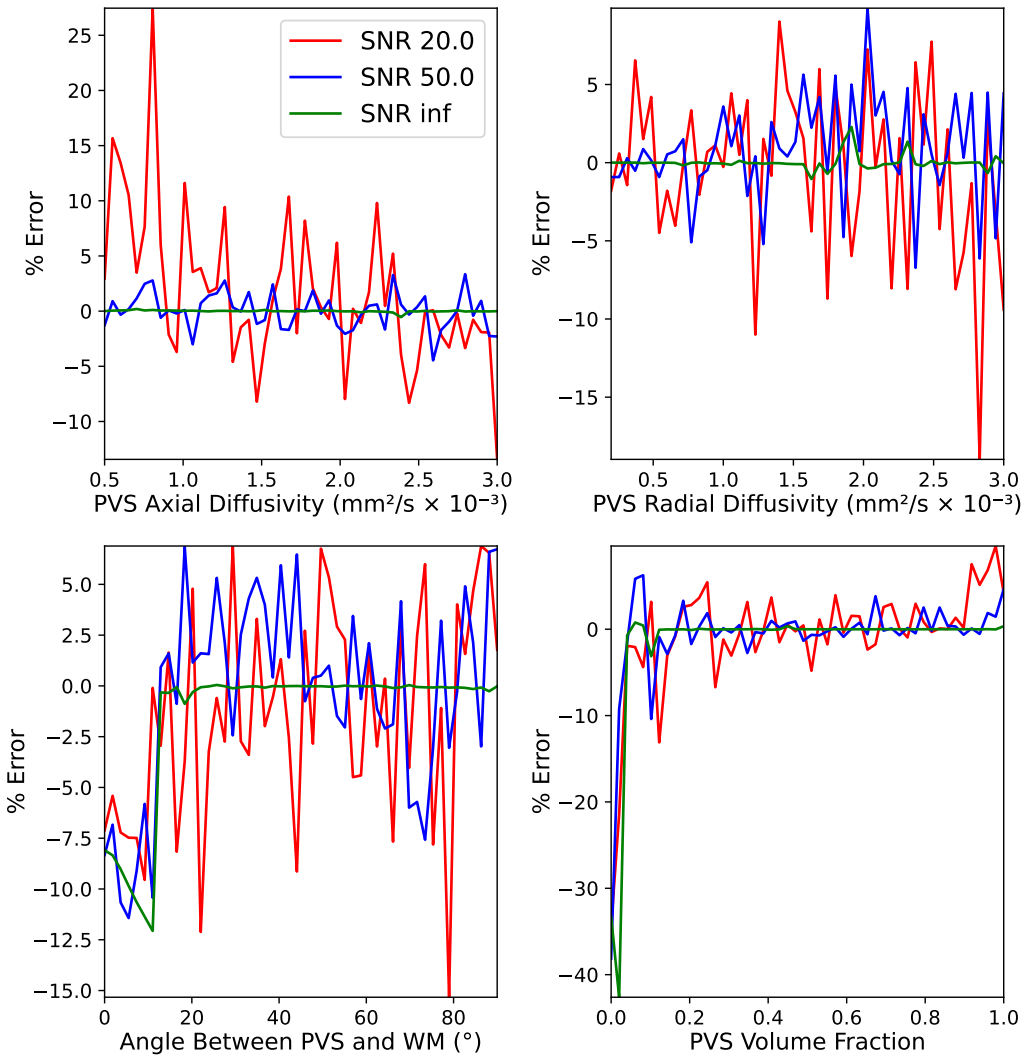


**FIGURE A.3: Simulation of Multi Compartment Constrained Tensor Reconstruction.** Error in estimating axial diffusivity using the recovered tensor is compared against the ground truth axial diffusivity. There appears to be no non-linear effects from decreased SNR.

---

<b>Subject</b>	<b>EPC-0.5</b>	<b>EPC-1.5</b>	<b>WPSS</b>	<b>Notes</b>
Average	2.9	1.45	4.4	–
102109	3	2	4	–
102614	2	1	5	–
102715	2	1	5	–
106824	4	2	5	–
111211	3	1	5	–
113316	3	1	5	Very enlarged PVS.
117021	4	2	4	–
118831	3	2	5	–
120414	2	1	4	–
123723	1	1	2	Unusually bright.
125222	3	2	4	Strong contrast.
125424	3	1	5	Very enlarged PVS.
126426	4	2	5	–
127226	3	1	5	–
130720	2	1	5	–
135124	4	2	4	–
135629	3	2	4	Clearer PVS in Centrum Semiovale.
138332	2	0	4	Darker image.
139435	1	1	3	Extreme PVS enlargement.
143224	1	1	5	–
146735	4	2	5	Lopsided appearance.
147636	4	2	4	–
151324	3	1	4	Minimal visible PVS.
151930	3	1	4	–
152225	4	2	4	–
152427	3	1	5	–
153126	4	3	5	–
161832	4	2	5	–
168947	2	1	4	–
169545	3	2	4	–

---

TABLE A.1: Visual Scoring of Perivascular Space Segmentation

# Bibliography

- [1] Kaylene Gouveia-Freitas and António J. Bastos-Leite. Perivascular spaces and brain waste clearance systems: relevance for neurodegenerative and cerebrovascular pathology. *Neuroradiology*, 63(10):1581–1597, 2021-10.
- [2] William Pham, Miranda Lynch, Gershon Spitz, Terence O'Brien, Lucy Vivash, Benjamin Sinclair, and Meng Law. A critical guide to the automated quantification of perivascular spaces in magnetic resonance imaging. *Frontiers in Neuroscience*, 16:1021311, 2022-12-14.
- [3] Toshiaki Taoka, Yoshitaka Masutani, Hisashi Kawai, Toshiki Nakane, Kiwamu Matsuoka, Fumihiko Yasuno, Toshifumi Kishimoto, and Shinji Naganawa. Evaluation of glymphatic system activity with the diffusion MR technique: diffusion tensor image analysis along the perivascular space (DTI-ALPS) in alzheimer's disease cases. *Japanese Journal of Radiology*, 35(4):172–178, 2017-04.
- [4] Nadia Aalling Jessen, Anne Sofie Finmann Munk, Iben Lundgaard, and Maiken Nedergaard. The glymphatic system: A beginner's guide. *Neurochemical Research*, 40(12):2583–2599, 2015-12.
- [5] E T Zhang, C B Inman, and R O Weller. Interrelationships of the pia mater and the perivascular (virchow-robin) spaces in the human cerebrum. *Journal of Anatomy*, 170:111–123, 1990-06.
- [6] Jesse M. Klostranec, Diana Vucevic, Kartik D. Bhatia, Hans G. J. Kortman, Timo Krings, Kieran P. Murphy, Karel G. terBrugge, and David J. Mikulis. Current concepts in intracranial interstitial fluid transport and the glymphatic system: Part i—anatomy and physiology. *Radiology*, 301(3):502–514, 2021-12.
- [7] Lulu Xie, Hongyi Kang, Qiwu Xu, Michael J. Chen, Yonghong Liao, Meenakshisundaram Thiagarajan, John O'Donnell, Daniel J. Christensen, Charles Nicholson, Jeffrey J. Iliff, Takahiro Takano, Rashid Deane, and Maiken Nedergaard. Sleep Drives Metabolite Clearance from the Adult Brain. *Science (New York, N.Y.)*, 342(6156):10.1126/science.1241224, October 2013.
- [8] Sanghyup Lee, Roh-Eul Yoo, Seung Hong Choi, Se-Hong Oh, Sooyeon Ji, Jongho Lee, Ki Young Huh, Ji Ye Lee, Inpyeong Hwang, Koung Mi Kang, Tae Jin Yun, Ji-hoon Kim, and Chul-Ho Sohn. Contrast-enhanced MRI T1 Mapping

- for Quantitative Evaluation of Putative Dynamic Glymphatic Activity in the Human Brain in Sleep-Wake States. *Radiology*, 300(3):661–668, September 2021. Publisher: Radiological Society of North America.
- [9] Benjamin T. Kress, Jeffrey J. Iliff, Maosheng Xia, Minghuan Wang, Helen Wei, Douglas Zeppenfeld, Lulu Xie, Hongyi Kang, Qiwu Xu, Jason Liew, Benjamin A. Plog, Fengfei Ding, Rashid Deane, and Maiken Nedergaard. Impairment of paravascular clearance pathways in the aging brain. *Annals of neurology*, 76(6):845–861, December 2014.
- [10] Paulien H. M. Voorster, Maud van Dinther, Willemijn J. Jansen, Alida A. Postma, Julie Staals, Jacobus F. A. Jansen, Robert J. van Oostenbrugge, Merel M. van der Thiel, and Walter H. Backes. Blood–Brain Barrier Disruption and Perivascular Spaces in Small Vessel Disease and Neurodegenerative Diseases: A Review on MRI Methods and Insights. *Journal of Magnetic Resonance Imaging*, 59(2):397–411, 2024. \_eprint: <https://onlinelibrary.wiley.com/doi/pdf/10.1002/jmri.28989>.
- [11] Farshid Sepehrband, Giuseppe Barisano, Nasim Sheikh-Bahaei, Ryan P. Cabeen, Jeiran Choupan, Meng Law, and Arthur W. Toga. Image processing approaches to enhance perivascular space visibility and quantification using MRI. *Scientific Reports*, 9(1):12351, August 2019. Number: 1 Publisher: Nature Publishing Group.
- [12] Giuseppe Barisano, Kirsten M. Lynch, Francesca Sibilia, Haoyu Lan, Nien-Chu Shih, Farshid Sepehrband, and Jeiran Choupan. Imaging perivascular space structure and function using brain MRI. *NeuroImage*, 257:119329, 2022-08-15.
- [13] I. C. George, A. Arrighi-Allisan, B. N. Delman, P. Balchandani, S. Horng, and R. Feldman. A Novel Method to Measure Venular Perivascular Spaces in Patients with MS on 7T MRI. *AJNR. American journal of neuroradiology*, 42(6):1069–1072, June 2021.
- [14] Sutton B. Richmond, Swati Rane, Moriah R. Hanson, Mehmet Albayram, Jeffrey J. Iliff, Dawn Kernagis, Jens T. Rosenberg, and Rachael D. Seidler. Quantification approaches for magnetic resonance imaging following intravenous gadolinium injection: A window into brain-wide glymphatic function. *European Journal of Neuroscience*, 57(10):1689–1704, 2023. \_eprint: <https://onlinelibrary.wiley.com/doi/pdf/10.1111/ejn.15974>.
- [15] Paulien H. M. Voorster, Maud van Dinther, Willemijn J. Jansen, Alida A. Postma, Julie Staals, Jacobus F. A. Jansen, Robert J. van Oostenbrugge, Merel M. van der Thiel, and Walter H. Backes. Blood–brain barrier disruption and perivascular spaces in small vessel disease and neurodegenerative diseases: A review on MRI methods and insights. *Journal of Magnetic Resonance Imaging*, 59(2):397–411, 2024-02. Publisher: John Wiley & Sons, Ltd.
- [16] Toshiaki Taoka, Rintaro Ito, Rei Nakamichi, Toshiki Nakane, Hisashi Kawai, and Shinji Naganawa. Diffusion tensor image analysis Along the perivascular

- space (DTI-ALPS): Revisiting the meaning and significance of the method. *Magnetic Resonance in Medical Sciences*, 23(3):268–290, 2024-04-02.
- [17] Matthew F. Glasser, Stamatios N. Sotiropoulos, J. Anthony Wilson, Timothy S. Coalson, Bruce Fischl, Jesper L. Andersson, Junqian Xu, Saad Jbabdi, Matthew Webster, Jonathan R. Polimeni, David C. Van Essen, and Mark Jenkinson. The minimal preprocessing pipelines for the human connectome project. *NeuroImage*, 80:105–124, 2013-10-15.
  - [18] Emily J. Allen, Ghislain St-Yves, Yihan Wu, Jesse L. Breedlove, Jacob S. Prince, Logan T. Dowdle, Matthias Nau, Brad Caron, Franco Pestilli, Ian Charest, J. Benjamin Hutchinson, Thomas Naselaris, and Kendrick Kay. A massive 7t fMRI dataset to bridge cognitive neuroscience and artificial intelligence. *Nature Neuroscience*, 25(1):116–126, 2022-01. Publisher: Nature Publishing Group.
  - [19] Alejandro F. Frangi, Wiro J. Niessen, Koen L. Vincken, and Max A. Viergever. Multiscale vessel enhancement filtering. In William M. Wells, Alan Colchester, and Scott Delp, editors, *Medical Image Computing and Computer-Assisted Intervention — MICCAI'98*, pages 130–137, Berlin, Heidelberg, 1998. Springer.
  - [20] Jesse M. Klostranec, Diana Vucevic, Kartik D. Bhatia, Hans G. J. Kortman, Timo Krings, Kieran P. Murphy, Karel G. terBrugge, and David J. Mikulis. Current Concepts in Intracranial Interstitial Fluid Transport and the Glymphatic System: Part I—Anatomy and Physiology. *Radiology*, 301(3):502–514, December 2021.
  - [21] Pascal P. R. Ruetten, Jonathan H. Gillard, and Martin J. Graves. Introduction to Quantitative Susceptibility Mapping and Susceptibility Weighted Imaging. *The British Journal of Radiology*, 92(1101):20181016, September 2019.
  - [22] Ryan P Cabeen, David H Laidlaw, and Arthur W Toga. Quantitative imaging toolkit: software for interactive 3d visualization, data exploration, and computational analysis of neuroimaging datasets. *ISMRM-ESMRMB Abstracts*, pages 12–14, 2018.
  - [23] José V. Manjón, Pierrick Coupé, Luis Martí-Bonmatí, D. Louis Collins, and Montserrat Robles. Adaptive non-local means denoising of MR images with spatially varying noise levels. *Journal of magnetic resonance imaging: JMRI*, 31(1):192–203, January 2010.
  - [24] Brian B. Avants, Nicholas J. Tustison, Jue Wu, Philip A. Cook, and James C. Gee. An Open Source Multivariate Framework for n-Tissue Segmentation with Evaluation on Public Data. *Neuroinformatics*, 9(4):381–400, December 2011.
  - [25] Haoyu Lan, Kirsten M. Lynch, Rachel Custer, Nien-Chu Shih, Patrick Sherlock, Arthur W. Toga, Farshid Sepehrband, and Jeiran Choupan. Weakly supervised perivascular spaces segmentation with salient guidance of Frangi filter. *Magnetic Resonance in Medicine*, 89(6):2419–2431, 2023. \_eprint: <https://onlinelibrary.wiley.com/doi/pdf/10.1002/mrm.29593>.

## BIBLIOGRAPHY

---

- [26] Wim Van Hecke, Louise Emsell, and Stefan Sunaert, editors. *Diffusion Tensor Imaging: A Practical Handbook*. Springer, New York, NY, 2016.
- [27] Bertram. Gradients in NMR spectroscopy – part 5: The pulsed gradient spin echo (PGSE) experiment.
- [28] J. Donald Tournier, Fernando Calamante, David G. Gadian, and Alan Connelly. Direct estimation of the fiber orientation density function from diffusion-weighted MRI data using spherical deconvolution. *NeuroImage*, 23(3):1176–1185, November 2004.
- [29] Ben Jeurissen, Jacques-Donald Tournier, Thijs Dhollander, Alan Connelly, and Jan Sijbers. Multi-tissue constrained spherical deconvolution for improved analysis of multi-shell diffusion MRI data. *NeuroImage*, 103:411–426, December 2014.
- [30] J.-Donald Tournier, Robert Smith, David Raffelt, Rami Tabbara, Thijs Dhollander, Maximilian Pietsch, Daan Christiaens, Ben Jeurissen, Chun-Hung Yeh, and Alan Connelly. MRtrix3: A fast, flexible and open software framework for medical image processing and visualisation. *NeuroImage*, 202:116137, November 2019.